Mineral assemblages and temperature associated with Cu enrichment in the Seival area (Neoproterozoic Camaquã Basin of Southern Brazil)

Rodrigo Lopes, Christophe Renac, Andre Mexias, Lauro V.S. Nardi, Eduardo Fontana, Marcia E.B. Gomes, Aurélie Barats

Mineral assemblages and temperature associated with Cu enrichment in the Seival area (Neoproterozoic Camaquã Basin of Southern Brazil)

Rodrigo W. LOPES[1–2], Christophe RENAC[2], André S. MEXIAS[1], Lauro V.S. NARDI[1], Eduardo FONTANA[3], Márcia E.B. GOMES[1], Aurélie BARATS[2]

[1] Universidade Federal do Rio Grande do Sul, Instituto de Geociências, avenida Bento Gonçalves, 9500, 91501–970 Porto Alegre, RS, Brazil

[2] Université Côte d'Azur, CNRS, IRD, Observatoire de la Côte d'Azur, Géoazur UMR 7329, 250 avenue Albert Einstein, 06560, Valbonne, France

[3] Universidade Federal dos Vales do Jequitinhonha e Mucuri, Centro de Geociências, Instituto de Ciência e Tecnologia, Rodovia MGT 367 – Km 583, nº 5000 – Alto da Jacuba, Diamantina, MG, Brazil

E–mail address: rodrigo.winck@ufrgs.br (R.W. Lopes), christophe.renac@unice.fr (C. Renac), andre.mexias@ufrgs.br (A.S. Mexias), lauro.nardi@ufrgs.br (L.V.S. Nardi), eduardo.fontana@ict.ufvjm.edu.br (E. Fontana), marcia.boscato@ufrgs.br (M.E.B. Gomes), aurelie.barats@unice.fr (A. Barats).

Abstract

The Neoproterozoic sequence of volcanic rocks in the Camaquã Basin included in the Lavras do Sul Shoshonitic Association hosts disseminated Cu deposits. The volcanic sequence in the Seival Mine area includes andesitic lava flows, lapilli tuff, volcanic agglomerate and andesitic dikes with pervasive alteration. The hydrothermal alteration is interpreted to be a product of late–magmatic fluids or the mixing of magmatic with meteoric fluids or basinal brines. The late–magmatic hydrothermal system started after volatile oversaturation and degassing in a magmatic system, which was partially segregated into vesicles. The similar REE contents in the andesine–labradorite and albite indicate that the fluid temperatures ranged from 600 to 250 °C. The crystallization of titanite and Fe–clinochlore to Mg–chamosite followed the albitization process. The temperature range associated with the chloritization process was estimated using a chlorite geothermometer

and varied from 251 ± 56 to 183 ± 39 °C. The precipitation of Mg–saponite and smectite–rich chlorite/smectite mixed–layers in some andesitic lava flows and the precipitation of quartz, calcite, barite and hematite in fractures suggest fluid circulation with temperatures lower than the chloritization process. The alteration minerals are represented by chlorite and albite associated with pyrite–chalcopyrite, while chlorite/smectite mixed–layers and barite or hematite are associated with bornite–chalcocite–covellite. Thermodynamic calculations confirm the potential coprecipitation of pyrite–chalcopyrite with chlorite and albite. The occurrence of bornite–chalcocite–covellite and barite seems to be favored by low–temperature chlorite/smectite with neutral to mildly acidic water influx. Consequently, albitization and the process of chloritization at high temperatures (> ca. 251 ± 56 °C) can be used as an exploration guide for primary pyrite–chalcopyrite enrichment, and chlorite/smectite at low temperatures (ca. 250 to 50 °C) can be related to bornite–chalcocite–covellite or the process of Cu enrichment.

Keywords: Late–magmatic and hydrothermal alteration; Albitization; Chlorites.

1. Introduction

The Neoproterozoic Camaquã Basin and its associated igneous rocks contain significant Au, Cu and Ag ore deposits, such as the Uruguay–São Luiz mines and the Lavras do Sul Mining District (Remus et al., 2000; Bongiolo et al., 2011; Renac et al., 2014). In the central–western section of this basin, volcanogenic (Lopes et al., 2014; Fontana et al., 2017) and plutonic rocks (Mexias et al., 2005) show pervasive alteration described as late–magmatic albitization and hydrothermal alteration with the influx of meteoric fluids (Mexias et al., 1990a, 2005; Bongiolo et al., 2011; Fontana et al., 2017). The largest Cu deposit in this basin is the Camaquã Mine, which is hosted in a Neoproterozoic sedimentary sequence and was exploited from the 18th century until 1996 (Remus et al., 2000; Laux et al., 2005; Renac et al., 2014). This exploited deposit has an ore reserve of ~30.8 Mt with an average Cu grade of ~1.06%, which is manifested as massive veins, stockworks and disseminated chalcopyrite, pyrite, bornite, chalcocite, gold, silver and hematite. The extrusive and intrusive rocks from the Lavras do Sul Mining District (Mexias et al., 2007), which are located on the central–western rim of the Camaquã Basin, host nineteen Au and Au–Cu deposits that were exploited during the same time frame (Bongiolo et al., 2011).

The ore zones consist of quartz and sulfide–rich quartz veins (Mexias et al., 2005) associated with wall–rock alteration characterized by 'sericite', chlorite, pyrite and chalcopyrite (Bongiolo et al., 2011). In the vicinity of the Lavras do Sul area, the volcanogenic sequence in the Seival area hosts Cu–Ag deposits (Reischl, 1978; Lopes et al., 2014). The different mines yielded ca. 0.20 Mt of Cu–ore with an average grade of ~1.40%. The chalcopyrite, pyrite, chalcocite, bornite and covellite sulfides occurred in association with chlorite, hematite, calcite, barite and quartz disseminated in andesitic lapilli tuff and volcanic agglomerates or along fault planes cutting the volcanic sequence. A recent study on the Seival Mine (Fontana et al., 2017) improved current knowledge about the clay minerals in these ore deposits. Fontana et al. (2017) described the zoning and lithotypes with the predominant occurrence of smectite, chlorite/smectite mixed–layers, chlorite and corrensite, and suggested that the base–metal deposition was related to the late–magmatic process of albitization and high–temperature hydrothermal alteration. Later low–temperature hydrothermal alteration represented the mixing of magmatic and meteoric fluids. Both albitization and chloritization processes were observed in the granite–related epithermal systems of the Lavras do Sul area (Mexias et al., 2007; Bongiolo et al., 2011) and the Camaquã Mine (Laux et al., 2005; Renac et al., 2014). A similar alteration mineralogy in the vicinity of the Lavras do Sul Intrusive Complex, located 10 km west of the Seival area, suggests that the Lavras do Sul porphyry–epithermal system contributes to the alteration of the andesitic rocks and ore deposition in the Seival area, as also occurs in the Potrerill Cu–Mo porphyry deposits and El Hueso Au epithermal deposits (Sillitoe, 1991; Marsh et al., 1997).

Consequently, this study focused on the chemical signatures of albite and chlorite to smectite in the hydrothermal alteration products. The petrographic and chemical analyses of the minerals were used to estimate the temperatures and bracket temperatures of late–magmatic to hydrothermal alteration. Petrographic observations and temperatures estimated by chlorite geothermometers were introduced into a thermodynamic model. This model was used to reconstruct the chemical conditions favorable to ore deposition in the process of base–metal migration in the Seival area.

2. Geological Setting

2.1 Regional geology

The Mantiqueira Province extends from the southeast of Brazil to Uruguay (Almeida and Hasui, 1984; Silva et al., 2005). In the Gondwana supercontinent, the southern portion of collision between the Rio de La Plata (Brazil) and the Kalahari (Africa) cratons is characterized by the Sul–rio–grandense Shield (Fig. 1A) with Neoproterozoic ages. This collision is represented by the Braziliano Orogeny and the opening of the Camaquã Basin related to the post–collisional stage (Lima and Nardi, 1998; Gastal et al., 2005a, b). The Sul–rio–grandense Shield comprises four geotectonic units: the Taquarembó Terrane, São Gabriel Terrene, Tijucas Terrene, and Pelotas Batholith. Recovering these units, the Camaquã Basin was considered as a succession of sub–basins (Paim et al., 2000) that contains volcano–sedimentary sequences. The Maricá Group, which is represented by the volcano–sedimentary rocks of the Maricá Formation, is related to a foreland retro arc–basin setting (630–601 Ma; Paim et al., 2000; Borba et al., 2008). The Bom Jardim Group, in which shoshonitic volcanism was emplaced during the strike–slip movement of the basin (600–590 Ma; Janikian et al., 2008), is represented by the Hilário Formation. The late Santa Bárbara Group (574–544 Ma; Sommer et al., 2006; Bicca et al., 2013; Almeida et al., 2012; Janikian et al., 2012; Matté et al., 2016) is mainly represented by the acidic effusive/explosive episodes and minor basic magmatism of the Acampamento Velho Formation and by the sedimentary sequences of the Santa Fé and Santa Bárbara formations (Fig. 1B). The Guaritas Group (547–535 Ma; Almeida et al., 2012; Oliveira et al., 2014) is represented by volcanic rocks of the Rodeio Velho Formation associated with a sedimentary sequence represented by the Pedra Pintada and Guaritas formations related to transtensional tectonic stages (Paim et al., 2000; Almeida et al., 2012). These effusive rocks have basic to intermediate sodic compositions with mildly alkaline to high–K tholeiitic affinities (Almeida et al., 2012).

INSERT Figure 1

The volcano–sedimentary units that occur in the Seival area (Fig. 2) have dominant intermediate compositions with basic and acidic end–members. The Bom Jardim Group, as previously described, consists of the effusive units of the Hilário Formation in the study

125 area (Ribeiro and Fantinel, 1978). The deformation of the Hilário Formation along the
126 Lavras do Sul contact suggests that the Hilário Formation is older than the Lavras do Sul
127 Intrusive Complex (Gastal et al., 2015). The Hilário Formation consists of dominantly
128 andesitic rocks represented by andesitic lava flows, lapilli tuff, volcanic agglomerates, and
129 dikes with a shoshonitic geochemical affinity (Lopes et al., 2014; Fontana et al., 2017). The
130 Ar–Ar radiogenic dating of plagioclase suggests an age of 600 to 590 Ma (Janikian et al.,
131 2008) that might be thermally influenced by intrusive magmas such as dikes or the Lavras
132 do Sul granitoids. The other vesicular lava flows and volcanic clastic materials are
133 represented by the polymictic conglomerates of the Santa Fé Formation. The Acampamento
134 Velho Formation occurs as rhyolite dikes that cross–cut the Hilário Formation.
135
136 **INSERT Figure 2**
137
138 The granitoids of the Lavras do Sul Intrusive Complex with U–Pb ages varying from
139 601 to 587 Ma (SHRIMP in zircon, Remus et al., 1999, 2000; Gastal et al., 2006; Liz et al.,
140 2009), comprise a ring structure composed of porphyritic quartz–monzonite granodiorite
141 and syenogranite to monzogranite with monzonitic intrusions in its northeastern margin
142 (Gastal et al., 2006; Liz et al., 2009). In the contact zone between the Lavras do Sul
143 granitoids and the Hilário Formation is a hectometer-thick metamorphic halo (Mexias et al.,
144 1990a, b; Bongiolo et al., 2011) attesting to the thermal influence of granitoids on the
145 volcano–sedimentary pile.
146
147 **2.2 Ore geology**
148 The Seival hosts six inactive Cu–bearing deposits and several prospects. This reserve
149 was estimated at ~0.20 Mt of ore with an average grade of ~1.40% of Cu and 10–70 ppm of
150 Ag (Fig. 3A; Reischl, 1978; Lopes et al., 2014). The ore deposits in the Seival area were
151 associated with the development of NE–SW-oriented shear zones that cross-cut the
152 Camaquã Basin (Fernandes et al., 1992; Philipp et al., 2016). The emplacement of metallic
153 mineralizations are bracketed between 600 and 580 Ma ago based on the ages of lava flows
154 (Janikian et al., 2008), tectonic activity (Gastal et al., 2015) and the Lavras do Sul
155 magmatism (Gastal et al., 2006; Almeida et al., 2012).

156 The sulfides are represented by chalcopyrite, bornite, chalcocite and covellite (Fontana
157 et al., 2017) and are part of the main Cu–bearing veins that fill fractures and faults. The
158 alteration halos are related to the distances of mineralized structures (Lopes et al., 2014;
159 Fontana et al., 2017). The mineral association of chlorite, epidote and calcite formed at
160 temperature of ~300 °C (Mexias et al., 1990b; Mexias et al., 2007; Bongiolo et al., 2011) in
161 the volcanogenic rocks of the Hilário Formation close to the Lavras do Sul granitoids.
162 The mineral assemblages allow for the characterization of hydrothermal zones
163 (Seedorff et al., 2005; Sillitoe, 2010). Propylitic alteration was related to chlorite, C/S
164 mixed–layer, hematite, titanite, calcite, barite and quartz associated with pyrite–
165 chalcopyrite and chalcocite–bornite, while argillic alteration was related to smectite and
166 quartz (Fig. 3B; Lopes et al., 2014; Fontana et al., 2017). Cu enrichment was associated
167 with propylitic alteration and the formation of albite (600 to 250 °C; Fontana et al., 2019)
168 and Mg–chamosite to Fe–clinochlore (251 to 180 °C). The late–hydrothermal veins are
169 composed of barite, calcite and minor proportion of veins with calcite–quartz assemblage.
170 These late precipitations represent the lowest temperatures of hydrothermal alteration (150
171 to 80 °C; Fontana et al., 2017). In the preserved parts of these inactive mines,
172 mineralization occurs as a stockwork of veins or disseminated in volcaniclastic rocks and
173 andesitic lava flows (Fontana et al., 2017). The faults, mineralized structures and dikes are
174 considered contemporaneous based on the mineralogy and alteration type. Thus, the
175 hydrothermal processes can be associated with the intrusion of NE–SW-oriented andesite
176 (Lopes et al., 2018) and local hydrothermal cells.
177
178 **INSERT Figure 3**
179
180 **3. Analytical methods**
181 Field work consisted of sample collection and logging of drill cores. The samples
182 collected were representative of lapilli tuff, amygdaloidal to porphyritic andesitic lava
183 flows and dikes. Petrographic observations of thin sections allowed the description of
184 magmatic and hydrothermally altered crystals. The minerals, after of crushing and sieving,
185 were separated using a magnetic separator, heavy liquids and hand–picking under a
186 binocular microscope. Products of alteration were either collected under a binocular

187 microscope in the altered phenocrysts or identified in the clay–size fraction. These
188 petrographic observations, mineral separation and clay–size fraction were characterized by
189 scanning electron microscopy combined with energy–dispersive spectrometry (SEM–EDS,
190 Zeiss EVO LS15, 20 kV, 2.5 nA with X–Max Oxford EDS detectors, IAEA Monaco) and
191 X–ray diffraction (Siemens D5000, KαCu, 40 kV and 25 mA, Geoscience Institute–CPGq–
192 UFRGS). X–ray patterns of the clay minerals were obtained in < 0.4 μm clay–size fraction.
193 Major element composition as oxides (SiO_2, TiO_2, Al_2O_3, FeO_{total}, MnO, MgO, CaO, Na_2O,
194 F and K_2O) in minerals from thin section were quantified by electron microprobe
195 (CAMECA, SXFive model equipped with TAP, PET and LIF crystal detectors) at the
196 Geoscience Institute, Universidade Federal do Rio Grande do Sul, Brazil. The beam
197 diameter is about 10 to 4 μm with an acceleration voltage of 15 kV and 15 nA with
198 counting time per element of 10 sec and background counting times of 5 sec per element.
199 Chemical calibrations were performed on albite, jadeite, diopside, sanidine, rutile,
200 rhodonite and hematite standards mounted in epoxy resin. The mineral composition in thin
201 section were calculated of atom per formula unit (a.p.f.u.) assumed the following number of
202 oxygen atoms for ideal compositions of feldspar (32), pyroxene (12), biotite (22), titanite
203 (5), smectite (22), chlorite/smectite mixed–layer (28) and chlorite (28). Charge balance of
204 structural formula was obtained by the adjustment of Fe^{2+} and Fe^{3+} proportions, including
205 for smectite and biotite, where only Fe^{2+} was considered. Analyzes in ten thin sections were
206 performed to follow changes from preserved magmatic minerals to mineral transformed or
207 precipitated by the hydrothermal alteration. Based on major element compositions,
208 chemical changes will then be related to albitization and chloritization processes. The
209 complete dataset of primary and hydrothermal minerals analyzed are available in
210 Supplementary Table A–G.
211 The major element changes observed in plagioclase were completed by rare earth
212 elements (REE; lanthanides, Y and Sc) analyzes. These REEs have been measured from
213 plagioclase separates preliminary recovered for phenocrysts and the microlithic
214 groundmass subsequently recognized with different major element compositions. These
215 REE concentrations were measured from feldspar separates preliminary acid leached with
216 ultrapure HNO_3 (1N) to dissolve traces carbonates and oxides on the surface of the grains
217 separated then clean in ultrapure pure MQ water. Later, cleaned grains were then acid

digested in ultrapure HNO_3 (15N) and HF (20N). Inductively–coupled plasma mass spectrometry analyzed all digested samples diluted in 1% HNO_3 solutions (ICP–MS: Elan DRCII, Perkin Elmer at the University of Nice Sophia–Antipolis). Quantification limits are below 50 ng/L. Element concentration was expressed as ppm and then normalized with respect to chondrite values (McDonough and Sun, 1995). The Eu* the values of the Eu anomaly were calculated using $[Eu^*]= [((Eu_N)/(Sm_N \times Gd_N)^{1/2})]$ from Worrall and Pearson (2001) or $[Eu^*] = [((Eu_N)/(Sm_N^2 \times Tb_N)^{1/3})]$ from Lawrence and Kamber (2006).

The different mineralogical and chemical data of magmatic minerals were used with the petrogenetic model (MELTS software modeling; Ghiorso and Sack, 1995) to reconstruct magmatic conditions. The magmatic and hydrothermal minerals were combined in a thermodynamic model (PHREEQC interactive; Parkhurst, 1995) to estimate the favorable conditions for precipitation of hydrothermal phases and sulfides.

4. Results

4.1 Textures and petrographic observations

The host rocks of the Cu deposits in the Seival area are predominantly andesitic lava flows and lapilli tuff (Fig. 4A) to volcanic agglomerates with rounded andesitic pyroclasts. Their aphyric groundmasses are dark to glassy and green with disseminated microlites of plagioclase and fragments of pyroxene. Amygdaloidal and porphyritic andesitic lava flows are predominant in the southern and northeastern parts of the Seival area and are in contact with the Santa Fé Formation (Fig. 2). Subvolcanic rocks have andesitic (Fig. 4B) to trachyandesitic compositions with feldspar phenocrysts, dominant pyroxene and scarce biotite phenocrysts.

Most of the rocks are intensively fractured and brecciated, particularly those with higher Cu sulfide contents. The andesitic pyroclasts in the lapilli tuff show vesicles or amygdaloids. The amygdaloidal groundmass in the lapilli tuff consists of fragments of igneous plagioclase and pyroxene. The petrographic observations of pyroxene revealed the replacement by clay minerals and calcite or intergranular spaces filled by clay minerals, quartz, calcite, titanite, pyrite, chalcopyrite, and minor hematite (Fig. 4C).

Porphyritic andesitic lava flows have phenocrysts of plagioclase and clinopyroxene in a trachytic groundmass with oriented plagioclase. Andesitic dikes host subhedral grains

of feldspars further identified as plagioclase with rims of K–feldspar (Fig. 4D) and phenocrysts of pyroxene. Some trachyandesitic dikes have subhedral phenocrysts of plagioclase, pyroxene and biotite. Some plagioclase and biotite phenocrysts have inclusions of apatite, zircon (50 to 200 μm) and titanite, while the oxidized groundmass contains hematite. The titanite grains occur as euhedral grains associated with biotite and pyroxene and as anhedral grains of smaller granular agglomerates in the altered groundmass.

As previously described (Lopes et al., 2014; Fontana et al., 2017), the Hilário volcanic sequence in the studied area is pervasively altered to clay minerals, calcite, barite and quartz. The original igneous mafic minerals and different groundmasses have a light green material recognized as chlorite/smectite mixed–layer (Fig. 4E). Albite, chlorite and sulfide occur in the more altered rocks with traces of calcite and specular hematite, and euhedral or agglomerates of titanite occur with albite and microscopic euhedral quartz (Fig. 4F).

Less-altered material occurs in the amygdaloidal andesitic lava flows from the south and west. Nevertheless, these lava flows are partially altered to dark clay minerals (Fig. 4G) between crystals or exhibit quartz, pyrite–chalcopyrite and calcite filling vesicles. Petrographic observations indicate the predominance of clay minerals associated with sulfides in the intergranular porosity that are further recognized as chlorite and dominant pyrite–chalcopyrite, or the association of chlorite/smectite mixed–layer (Fig. 4H) with minor pyrite–chalcopyrite and dominant chalcocite–covellite or chalcocite–bornite. The malachite and azurite observed in the different open pits are the product of the recent weathering of Cu–rich sulfides.

INSERT Figure 4

4.2 Major element compositions of magmatic to late–magmatic minerals and REE compositions of feldspars

Phenocrysts and microlites or crystalloclasts of pyroxene in porphyritic andesitic lava flows and andesitic dikes are augite ($Wo_{0.40–0.47}$ $En_{0.32–0.41}$ $Fs_{0.12–0.28}$; Fig. 5A; Supplementary Table A). According to the structural formula of augite (Table 1), the atomic

ratios of [Mg/(Mg+Fe_{tot})= 0.67–0.85] are high and those of [Na/(Ca+Na)= 0.02–0.05)] are low.

Prismatic biotite phenocrysts recognized in trachyandesitic dikes are classified as Mg–biotite with the structural formula expressed in Supplementary Table B. The less pristine Mg–biotites show slightly different compositions (Table 1), with increases in Al^{VI} (Fig. 5B) and lower contents of Fe, Mg and Mn (Table 1). The euhedral to agglomerate titanite grains (Fig. 5C; Table 1 and Supplementary Table C) are associated with albite and biotite phenocrysts, and the anhedral grains in the groundmass have similar chemical compositions.

The chemical compositions of feldspars were analyzed in thin section. The plagioclase phenocrysts have compositions of andesine–labradorite ($An_{0.43–0.53}$ $Ab_{0.43–0.54}$ $Or_{0.03–0.05}$) (Table 1). Moreover, some of the andesine–labradorite phenocrysts have a thin rim of K–feldspar ($An_{0–0.01}$ $Ab_{0–0.33}$ $Or_{0.66–1}$; Fig. 4B and Fig. 5D; Table 1), further described as Group I. In contrast, the microlites and phenocrysts of plagioclase (Supplementary Table D) from altered lapilli tuff, porphyritic andesitic lava flows and andesitic dikes consist of dominant albite ($An_{0–0.06}$ $Ab_{0.89–1}$ $Or_{0–0.10}$; Table 1), further described as Group II. The feldspar separates were characterized by X–ray diffraction and observed by SEM–EDS. The separates with traces of illite or quartz were removed from further REE measurements. The total REE content of andesine–labradorite (Group I) and albite (Group II) have similar patterns and are slightly higher in albite. However, the andesine–labradorite (Group I) and albite (Group II) have both positive have positive Eu anomalies (Group I: [Eu*]= 0.90–1.22; Group II: [Eu*]= 1.04–4.60; Table 2).

INSERT Figure 5

INSERT Table 1

INSERT Table 2

4.3 Mineralogy and major elemental compositions of clay minerals

Petrographic observations show “green clays” replacing pyroxene, biotite or feldspars that fill vesicles and intergranular porosity. Similar to Fontana et al. (2017), using X–ray diffraction techniques on clay–size fractions allowed for the identification of

dominant trioctahedral smectite and smectite–rich (C/S) in less altered andesitic lava flows, as well as chlorite–rich chlorite/smectite mixed–layer and chlorite in more altered andesitic lava flows and lapilli tuff. The occurrence of different clay minerals for similar andesitic lithotypes suggests that hydrothermal alteration is not completely related to the primary magmatic mineralogy but to the influx of external fluid. The in–situ electron microprobe analyses allowed for the identification of the composition of the large chlorite flakes (Fig. 6) in the cleavage of andesine–labradorite and albite and the replacement of augite phenocrysts or micrometer vugs in the andesitic dikes with a light green color (Table 1). Based on the $Fe^{2+}/(Fe^{2+}+Mg)$ ratio, these chlorites have compositions of Fe–clinochlore to Mg–chamosite (Supplementary Table E). The observed $Fe^{2+}/(Fe^{2+}+Mg)$ atomic ratios between 0.47 and 0.64 suggest that values < 0.5 are Fe–clinochlore and those of > 0.5 are Mg–chamosite. These two types of chlorite were also recognized in a regional epithermal system (Fig. 7; Mexias et al., 1990b; Bongiolo et al., 2011) and distal–epithermal halo from the Camaquã Mine (Fig. 7; Troian et al., 2010; Renac et al., 2014). Low $Fe^{2+}/(Fe^{2+}+Mg)$ proportions are structurally compensated by tetrahedral and octahedral aluminum (Al^{IV}= 1.7 to 3.4; Al^{VI}= 2.7 to 3.11). The Fe–clinochlore to Mg–chamosite in andesitic lava flows and lapilli tuff have lower Fe^{2+}+Mg atomic proportions (7.5 to 8.5; atomic ratios of $Fe^{3+/}Fe_{tot}$= 0.01 to 0.06) than in andesitic dikes (Fe^{2+}+Mg= 9 to 10.1; atomic ratio of Fe^{3+}/Fe_{tot}= 0.05). However, the chloritization of augite and filling of vugs reflect increasing contents of Fe+Al and Fe+Mg total contents in lapilli tuff and andesitic dikes, respectively. In addition, the Fe–clinochlore to Mg–chamosite compositions are very similar (Fig. 8A; Table 1) and were described using the same structural formula.

INSERT Figure 6

INSERT Figure 7

INSERT Figure 8

The occurrence of dominant chlorite/smectite, trioctahedral smectite and corrensite recognized by their dark green color and identified using X–ray diffraction (Fig. 8) was confirmed by electron microprobe measurements. The smectite–rich chlorite/smectite, smectite (Supplementary Table F) and corrensite (Fig. 8B and Figs. 9A–B) represent the

dominant hydrothermal phase of andesitic lava flows and andesitic dikes. The dominant trioctahedral smectite (Fig. 8C) has a Mg–saponite composition (Table 1). The dominant chlorite–rich chlorite–smectite (Fig., 8D; Supplementary Table G) with micrometer-scale fan–shaped particles (Fig. 4C) occurs in altered porphyritic and amygdaloidal andesitic lava flows. The chlorite–rich chlorite–smectite have Al^{VI} and ^{IV} contents (Al_{tot} 2.21+ 1.25 to 2.46+ 1.48 a.p.f.u.) that are higher in the porphyritic andesitic lava flows than the chlorite–rich chlorite–smectite (Al_{tot}= 1.59+ 0.77 to 1.93+ 1.47) in the amygdaloidal andesitic lava flows. The proportion of Fe and its valency balance are represented by changes in tetrahedral and octahedral Al. The chlorite–rich chlorite–smectite structural formulas vary between porphyritic and amygdaloidal andesitic lava flows (Table 1).

INSERT Figure 9

It is possible to confirm the association of albite and chlorite minerals with Cu enrichment. The magmatic and post–magmatic stages were related to albite and chlorite crystallization, while chlorite, chlorite/smectite mixed–layer and the destabilization of sulfides were related to the precipitation of chalcocite–bornite. These mineral associations suggest a sequence of crystallization and hydrothermal alteration over time.

5. Discussion

5.1 Chemistry of magmatic and late–magmatic minerals

The volcanogenic rocks in the Seival area are interpreted as part of the Lavras do Sul Shoshonitic Association (Lima and Nardi, 1998), which are related to the Lavras do Sul granitoids and lamprophyres. The occurrence of lamprophyres (Lima and Nardi, 1998; Almeida et al., 2012), andesitic dikes and various volcanic events in the region suggests long and intense episodes of magmatism in the Seival area constrained by the dating of zircon (Almeida et al., 2012; Janikian et al., 2012) between 600 ± 2 to 590 ± 6 Ma. The mineralogy of andesitic rocks with andesine–labradorite, augite and Mg–biotite phenocrysts and their whole–rock compositions (Lima and Nardi, 1998; Sommer et al., 2006; Lopes et al., 2014) suggest a petrogenetic link with the Lavras do Sul Shoshonitic Association.

Petrogenetic modeling (MELTS Software: Ghiorso and Sack, 1995) used with whole–rock compositions (Lopes et al., 2014) estimates a liquidus temperature of ca. 1080 °C. The modeling shows a sequence of crystallization initiated by calcic plagioclase followed by low–Ca–pyroxene, late orthoclase and high–Ca pyroxene or biotite (ca. 800 °C). The stages below 800 °C include late–magmatic minerals formed by volatile-rich melt (c.f. Dixon et al., 1995). In this context, the biotites observed with the higher Al^{IV} contents of less pristine biotite compared with the biotite phenocrysts might represent two stages of biotite crystallization or slightly altered crystals. The late–magmatic stage initiated at solidus temperatures (800 to 500 °C) with volatile oversaturation and the degassing of the melt (c.f. Dixon et al., 1995). This interpretation is reinforced by the oxygen isotopic values of andesine–labradorite ($\delta^{18}O_{\text{andesine–labradorite}}$: 6.6 to 8.2 ‰; Fontana et al., 2019) showing the magmatic signature of fluids in equilibrium with feldspars (Taylor, 1987) evolving toward the mixing of meteoric and magmatic fluids for albite ($\delta^{18}O_{\text{albite}}$: 14.2 to 16.2 ‰; Fontana et al., 2019). Consequently, presume that observed Mg–biotite formation, euhedral F–rich titanite grains and albite are related to late–magmatic crystallization and albitization processes of andesine–labradorite. According to thermodynamic modelling and the literrature (c.f. Higgins and Ribb, 1976; Franz and Spear, 1985; Enami et al., 1993; Tropper et al., 2002; Harlov et al., 2006; Hövelmann et al., 2010; Kaur et al., 2012) this albitization process occurs at temperatures below 800 °C, presumably from ca. 600 to 250 °C. The widely observed albite suggests a magmatic to high–temperature hydrothermal system (epithermal–porphyry: Richards, 2003; Sillitoe, 2010 or Iron Oxide–Copper–Gold; Sillitoe, 2003; Williams et al., 2005; Groves et al., 2010). The alkaline and acidic fluids in these systems are related to the albitization process and K–rich alteration (Perez and Boles, 2005; Boulvais et al., 2007) that, to some degree, participated or started the leaching of base metals from the lava (Moody et al., 1985; Perez and Boles, 2005; Hövelmann et al., 2010; Kontonikas–Charos et al., 2014). Non-magmatic basinal brine has also reported in the albitization process (Barton and Johnson, 1996 and 2000), such as in the Nevada porphyry, IOCG deposits (Carten, 1986; Dilles and Einaudi, 1992; Dilles et al., 2000; Sillitoe, 2003; Mark et al., 2006; Kendrick et al., 2007) or Chilean “Manto–type” deposits, such as Michilla, with the mixing of magmatic and basinal brine (Barton, 2014). In the Seival area, the change of andesine–labradorite ($An_{0.43–0.53}$ $Ab_{0.43–0.54}$ $Or_{0.03–0.05}$) to albite ($An_{0–0.06}$ Ab

$_{0.89–1}$ Or $_{0–0.10}$) with rare K–feldspar rims on andesine–labradorite or rare illite attest to the circulation of alkaline fluid. Moreover, the sizes of the quartz and calcite crystals with liquid inclusions did not allow fluid inclusion microthermometry to recognize high–density fluid, as in IOCG-type deposits (Reeve et al., 1990; Davidson and Large, 1998). The REE patterns of albite-rich separates (Group II: Eu*= 1.04–4.60) are similar to the whole–rock (Fig. 10; Lopes et al., 2014). The more positive Eu anomaly of group II and whole–rock (whole–rock: Eu*= 6.23) compared to Group I (Labradorite Eu*= 0.90–1.20). These overall, positive Eu positive anomalies (Eu*= >1; Table 2) higher in the albite (group II; Fig. 10A–B) than andesine–labradorite–rich grains (group I) seem unrealistic assuming, first crystallization of Ca–feldspar then Na–rich feldspar. However, the more positive Eu anomalies of whole–rock and Group II might be related to trace minerals such as apatite inclusions in plagioclase, as mentioned in the petrography section and whole–rock. These inclusions have not been remove totally by preliminary acid–leaching used to clean feldspars of carbonates, Ca–phosphates and Fe oxides (Fontana et al., 2017). The REE signature of Ca–rich feldspar would then represent a chronologically primitive signature in the magmatic chamber, while, the late crystallization include dominant Na–rich feldspar and phosphate traces.

Nevertheless, the similar □REE contents with LREE and HREE variations from albites and andesine–labradorite suggest a similar source of REE (□REE) that was not affected by fluid dilution, such as that by meteoric fluids. Therefore, the albitization process in the Hilário Formation was related to the neutral to mildly acidic water circulation of Na–rich magmatic fluid, such as late–magmatic glass interactions with outgassing magmatic fluids (CO_2 and H_2O), but these data cannot decipher between a magmatic to late–magmatic crystallization with the mixing of magmatic fluids and brine (e.g. IOCG: Barton and Johnson, 1996 and 2000).

INSERT Figure 10

No mineralization model has yet been proposed for the Seival Mine. Fontana et al. (2017) indicated mineralization associated with magmatic and meteoric fluids. The aligned Cu–Ag ore bodies and disseminated mineralizations (see Figure 3) with similar mineral

assemblages (albite, chlorite, chlorite/smectite mixed–layers, chalcocite–bornite, barite, and minor calcite, hematite and quartz) could be typical of epithermal deposits (Sillitoe, 2010) associated with the geothermal influence of andesitic dikes or the Lavras do Sul granitoids. These observations and interpretations suggest that Seival would be a superficial part of the Lavras do Sul porphyry (Mexias et al., 2007; Bongiolo et al., 2011). We assumed that low–hematite contents in the Seival area associated with calcite in small veins and ore deposits without an iron–oxide caprock are clues discarding the hypotheses of an IOCG type deposit or a metallic enrichment related to weathering profile such as Gossan genetic model of ore deposits.

5.2 Clay minerals and chlorite during hydrothermal stages

The hydrothermal stages associated with saponite, chlorite/smectite and chlorite precipitations surrounding albite suggest hydrothermal fluids of below 350 °C. Previous studies (Lopes et al., 2014; Fontana et al., 2017) characterized the occurrence of Fe–Cu–rich sulfides associated with chlorite/smectite. The association of Cu–rich sulfides with Fe –Al –Mg rich chlorite/smectite suggests that the Fe^{2+}, Mg and Al contents of the clay minerals are related to ore deposition (Wilkinson et al., 2015; Yoneda et al., 2016). Nevertheless, the origin, chemistry and temperature of the fluids are not well characterized.

In the Seival area, crystallography realized by X–ray diffraction and mineral chemistry obtained by electron electron microprobe analyses identified Mg–saponite (smectite), chlorite/smectite mixed–layer and corrensite infilling the porosity or intergranular spaces. The occurrence of dominant clay minerals with Mg–saponite, chlorite/smectite and corrensite in different lithotypes was interpreted as a lithological control of alteration rather than being derived from local equilibrium (Fontana et al., 2017). The comparison of the major element compositions of magmatic minerals (Part 4.2), clay mineral (part 4.3) and whole–rock samples (Lopes et al., 2014) provided information to support this hypothesis. The predominant Fe– Mg–rich clay minerals and their Fe_{tot}/Fe_{tot}+Mg atomic ratios compared to augite (0.14 to 0.27) and biotite (0.37 to 0.44) indicate that Mg–saponite (0.22 to 0.27) and chlorite/smectite mixed–layers may be derived from the alteration of magmatic minerals and glass. In contrast, the high Fe–clinochlore to Mg–chamosite ratio (0.47 to 0.63; Supplementary Table E) suggests the addition of Fe and

464 Mg during the chloritization process. This interpretation as confirmed by mass–balance
465 calculations performed by Fontana et al. (2019).
466 We estimated the temperatures of chlorites using chemical thermometers (Inoue et
467 al., 2009; Bourdelle and Cathelineau, 2015). These thermometers are the only available
468 temperature constraint considering the small sizes of the fluid inclusions (Fontana et al.,
469 2017). We discarded the chemical thermometer of chlorite related to metamorphic
470 conditions and selected one determined in similar lithotypes and pressure conditions. The
471 chosen chemical thermometers use a structural formula with an uncertainty dominantly
472 controlled by the Fe valency and different octahedral layers. Assuming an error of 20% in
473 the Fe distribution, the uncertainty is approximately 50 °C in both calculations. The
474 calculated temperatures of Fe–clinochlore to Mg–chamosite (Supplementary Table E) vary
475 from 129 to 275 °C in the lapilli tuff–andesite (median= 183 ± 39 °C; n= 18) and 172 to
476 312 °C in andesitic dikes (median= 251 ± 56 °C; n= 8). Moreover, the compositional
477 changes in chlorite in the Seival area compared to those in the Lavras do Sul area (Mexias
478 et al., 1990b; Bongiolo et al., 2011) or the Camaquã Mine (Renac et al., 2014) yield
479 comparable temperatures. These different uncertainties (± 50 °C) and calculated
480 temperatures reflect chloritization below of the minimum temperature of albitization. The
481 higher temperature of chlorite associated with andesitic dikes suggests a temperature
482 related to intrusive bodies or different thermal gradients between lapilli tuff and andesitic
483 dikes.
484
485 **5.3 Hydrothermal evolution and thermodynamic modeling**
486 The chlorite and chlorite/smectite mixed–layers associated with sulfides are typical
487 mineralogical assemblages of hydrothermal deposits (Barnes, 1979; Pirajno, 2009; Sillitoe,
488 2010). In the Seival area, different Fe–Cu –rich sulfide assemblages occur in the
489 intergranular space or are mixed with clay minerals (Fontana et al., 2017).
490 Hydrothermal alteration minerals are associated with a sequence of precipitations
491 rather than a paragenetic assemblage, as occurs in metamorphic reactions. Therefore,
492 thermodynamic modeling can be erroneous when based on the assumption of an output
493 represented by all of the hydrothermal phases observed. Consequently, we tested the
494 different equilibrium conditions of the hydrothermal stage (below 350 °C) with

thermodynamic modeling (PHREEQC interactive; Parkhurst, 1995, rather than SUPCRIT or the equivalent CHONZ Rpackage). The PHREEQC thermodynamic models primarily use minerals with an initial water content and propose secondary minerals as outputs with the new composition of the final fluid. In our case, reactions involved observed magmatic minerals observed (feldspars: andesine–labradorite and albite and Ca–pyroxene: augite) and late–magmatic minerals (biotite, titanite, Fe–titanium oxides and silica–rich glass) reacting with initial fluid (low–concentration water similar to rainfall, Salve et al., 2008), and carbonic fluids (CO_2 as recognized in fluid inclusions (Fontana et al., 2017). The temperature domain of these calculations was bracketed by the albitization process (< 350 °C) and the calculations of the chlorite thermometer (120 to 320 °C). Each calculation considers a molar proportion of water a hundred times higher than those of minerals and fluids for varying pH values and temperatures below 350 °C. Consequently, the thermodynamic changes in calculated fluids and the dissolution or precipitation of primary and secondary minerals equilibrated at 350, 300, 250, 200 and 150 °C with pH and Eh were adjusted for charge balance and redox conditions. These preliminary calculations indicate multiple solutions with more products than were identified in the altered rocks. Therefore, we forced the software to uniquely consider results with chlorite, calcite, quartz and Fe–Cu rich sulfide or barite, which are here assumed to be products of hydrothermal reactions, without any constraints related to their precipitation or dissolution.

These thermodynamic calculations were obtained for neutral (pH: 7) and acidic (pH: 4) initial water conditions. Regardless of the considered temperature, all final waters remained neutral for an initial fluid with a neutral pH (pH: 7 to 7.3), whereas acidic waters changed to a neutral pH (pH 4 to 7.3).

The high–temperature (350 °C) calculations indicate the coprecipitation of albite and titanite with the total consumption of the Ca–rich feldspars and pyroxene, but no minor chlorite or smectite. The conservation of some pyroxene and andesine–labradorite observed in the petrography and the lack of clay minerals suggests unrealistic solutions for hydrothermal alteration forming albite with titanite and chlorite. Consequently, we forced the precipitation of chlorites in a second data set.

– For temperatures between 350 and 250 °C, the chlorite, quartz and calcite associated with pyrite and chalcopyrite can be formed, whereas silica–rich glass, titanite and Ti–magnetite are consumed anorthite, albite and pyroxene are partially dissolved.

– For temperatures between 250 and 150 °C, neutral or acid water dissolved magmatic minerals with predicted precipitations of chlorite, barite, calcite, quartz and hematite with bornite–chalcocite. Mg–saponite (smectite) was precipitated below 200 °C.

– Below 150 °C, the lower activities of Fe^{2+} with decreasing $HS^-/(HS^-+SO_4)$ molar ratios increased the saturation with respect to chalcocite and sulfate and Fe oxides, such as barite and hematite. These calculations confirm that pyrite and chalcopyrite were probably precipitated from a dominant magmatic fluid at temperatures between 350 to 250 °C. The further mixing of the magmatic fluid with meteoric water or basinal brine at temperatures varying from 250 to 150 °C promoted chalcocite–bornite deposition. Considering the domain of barite saturation and the lack of supergene alteration or gossan profiles in this region, the lower temperature of the Cu enrichment of sulfide ranged from 150 to 50 °C.

6. Conclusions

The Seival area contains hydrothermal Cu–sulfide deposits hosted in volcanic rocks with a shoshonitic affinity. Interpretations based on mineralogical and chemical data suggest that volatile–rich magma produced Mg–biotite, followed by late–magmatic alteration with titanite and the albitization of andesine–labradorite (650 to 250 °C), as suggested by the REE contents of albite. Thermodynamic modeling indicates that late albitization (ca. < 350 °C) was associated with the formation of primary pyrite–chalcopyrite, or that high–temperature chloritization (350 to 250 °C) was associated with bornite–chalcocite. Moreover, the Fe_{tot}/Fe_{tot}+Mg atomic ratios of Fe–clinochlore to Mg–chamosite suggest that fluids altered the pyroxene or residual material with the addition of external Fe compared to smectite precipitation. The high Fe_{tot}/Fe_{tot}+Mg atomic ratios and high Fe^{2+}/Fe^{3+} atomic ratios of these chlorites suggest an Fe–rich and reduced fluid in agreement with the migration of Fe, Cu and S species producing sulfides. However, the origin of fluid, whether the mixing of magmatic and meteoric fluids or basinal brines (IOCG, Chilean ‘Manto type’), was not identified. Nevertheless, the chloritization process occurred from 312 to 120 °C. Despite the errors related to chlorite thermometers, the ranges

555 of temperatures in the lapilli tuff (275 to 129 °C; median= 183 ± 39 °C) and andesitic dikes
556 (312 to 172 °C, median= 251 ± 56 °C) suggest the existence of changing thermal gradients
557 related to the cooling of the lava pile or intrusive dike and fluids with different
558 temperatures at different times.
559 The lowest-temperature stage was related to the widespread formation of Mg–
560 saponite and smectite–rich C/S (200 to 50 °C). The formations of chlorites,
561 chlorite/smectite mixed–layers and Mg–saponite were related to the influx of fluids
562 (meteoric water or basinal brine) at lower thermal fluxes associated with the sulfide
563 assemblage of bornite–chalcocite, chalcocite, and barite with the increasing concentration
564 of sulfate. Consequently, the petrographic association of albite and chlorite with pyrite and
565 chalcopyrite suggests that the albitization to chloritization stage and structural control may
566 be prospective guides for Cu fertile magmatic systems. The chlorite/smectite mixed–layers
567 emphasized favorable Cu–enriched zones, such as fluid circulation in faults or along dikes
568 and percolation in the porosity of the lapilli tuff.

569

570 **Acknowledgements**

571 This study is part of the cotutelle doctoral thesis of Rodrigo Winck Lopes at
572 Universidade Federal do Rio Grande do Sul and Université Côte d´Azur. We wish to thank
573 the Conselho Nacional do Desenvolvimento e Pesquisa (CNPq), CAPES and Programa
574 Ciências Sem Fronteiras (Process number: 200081/2014–4) for financial support. We thank
575 Votorantim Metais for allowing access to drill–cores. We thank Robert Ayuso, Karel
576 Breiter, Douglas Kreiner, Bruno Lemiere, David Lentz and anonymous reviewer for their
577 constructive remarks during the reviewing and editing processes. We wish to thank Everton
578 Bongiolo and Maria José Mesquita for additional revision. We wish to thank the members
579 of the research group Marcelo Lindenberg, Bruno Petracco and the technician laboratory:
580 Denise Canarim, Susan Drago, Edgar Bercht and Lucas Jantsch.

581

582 **References**

583 Almeida, F.F.M., Hasuy, Y., 1984. O Pré–Cambriano do Brasil (Portuguese – Brazil).
584 São Paulo: Edgard Blücher, 378 p.

585 Almeida, D.P.M, Chemale Jr., F., Machado, A., 2012. Late to Post–Orogenic
586 Brasiliano–Pan–African volcano–sedimentary basins in the Dom Feliciano Belt,
587 Southernmost Brazil, in: Al–Juboury, A.I. (Ed.), Petrology – New Perspectives and
588 Applications, pp. 73–135.
589 Barnes, H.L., 1979. Geochemistry of Hydrothermal Ore Deposits. Second Edition,
590 Wiley–Interscience, Inc., New York, 798 p.
591 Barton, M.D., Johnson, D.A., 1996. Evaporitic source model for igneous–related Fe
592 oxide–(REE–Cu–Au–U) mineralization. Geology, 24, 259–262.
593 Barton, M.D., Johnson, D.A., 2000. Alternative brine sources for Feoxide(–Cu–Au)
594 systems: Implications for hydrothermal alteration and metals. In: Hydrothermal iron oxide
595 copper–gold and related deposits: A global perspective (Porter, T.M., editor). Adelaide,
596 Australian Mineral Foundation, pp. 43–60.
597 Barton, M.D., 2014. Iron oxide(–Cu–Au–REE–P–Ag–U–Co) systems. Treatise on
598 Geochemistry, 13, 515–541.
599 Bayliss, P., 1975. Nomenclature of the trioctahedral chlorites. The Canadian
600 Mineralogist, 13, 178–180.
601 Bicca, M.M., Chemale Jr., F., Jelinek, A.R., Oliveira, C.H.E., Guadagnin, F.,
602 Armstrong, R., 2013. Tectonic evolution and provenance of the Santa Bárbara Group,
603 Camaquã Mines region, Rio Grande do Sul, Brazil. Journal of South American Earth
604 Sciences, 48, 173–192.
605 Bongiolo, E.M., Renac, C., Mexias, A.S., Gomes, M.E.B., Ronchi, L.H., Patrier–
606 Mase, P., 2011. Evidence of Ediacaran glaciation in southernmost Brazil through magmatic
607 to meteoric fluid circulation in the porphyry–epithermal Au–Cu deposits of Lavras do Sul.
608 Precambrian Research, 189, 404–419.
609 Borba, A.W., Mizusaki, A.M.P., Santos, J.O.S., McNaughton, N.J., Ono, A.T.,
610 Hartmann, L.A., 2008. U–Pb zircon and ^{40}Ar–^{39}Ar K–feldspar dating of syn–sedimentary
611 volcanism of the Neoproterozoic Maricá Formation: constraining the age of foreland basin
612 inception and inversion in the Camaquã Basin of southern Brazil. Basin Research, 20, 359–
613 375.

614 Boulvais, P., Ruffet, G., Cornichet, J., Mermet., M., 2007. Cretaceous albitization and
615 dequartzification of Hercynian peraluminous granite in the Salvezines Massif (French
616 Pyrénées). Lithos, 93, 89–106.
617 Bourdelle, F., Cathelineau, M., 2015. Low–temperature chlorite geothermometry: a
618 graphical representation based on a T–R^{2+} diagram. European Journal of Mineralogy, 27,
619 617–626.
620 Cao, M.J., Qin, K.Z., Li, G.M., Evans, N.J., Jin, L.Y., 2015. Abiogenic Fischer–
621 Tropsch synthesis of methane at the Baogutu reduced porphyry copper deposit, western
622 Junggar, NW China. Geochimica et Cosmochimica Acta, 141, 179–198.
623 Carten, R.B., 1986. Sodium–calcium metasomatism; chemical, temporal, and spatial
624 relationships at the Yerington, Nevada, porphyry copper deposit. Economic Geology, 81,
625 1495–1519.
626 Davidson, G.J., Large, R.R., 1998. Proterozoic copper–gold deposits. AGSO Journal
627 of Australian Geology and Geophysics, 17, 105–113.
628 Dilles, J.H., Einaudi, M.T., 1992. Wall–rock alteration and hydrothermal flow paths
629 about the Ann Mason porphyry copper deposit, Nevada; a 6–km vertical reconstruction.
630 Economic Geology and the Bulletin of the Society of Economic Geologists, 87, 1963–
631 2001.
632 Dilles, J.H., Einaudi, M.T., Proffett, J.M., Barton, M.D., 2000. Overview of the
633 Yerington porphyry copper district: magmatic to nonmagmatic sources of hydrothermal
634 fluids, their flow paths, alteration affects on rocks, and Cu–Mo–Fe–Au ores. Society of
635 Economic Geologists, Post–Meeting Field Conference, 32, 55–66.
636 Dixon, J.E., Stolper, E.M., Holloway, J.R., 1995. An experimental study of water and
637 carbon dioxide solubilities in mid–ocean ridge basaltic liquids. Part 1: Calibration and
638 solubility models. Journal of Petrology, 36, 1607–1631.
639 Enami, M., Suzuki, K., Liou, J.G., Bird, D.K., 1993. Al–Fe^{3+} and F–OH substitution
640 in titanite and constraints on their P–T–dependence. European Journal of Mineralogy, 5,
641 219–231.
642 Fernandes, L.A., Tommasi, A., Porcher, C.C., 1992. Deformation patterns in the
643 Southern Brazilian branch of the Dom Feliciano Belt: a reappraisal. Journal of South
644 American Earth Sciences, 5, 77–96.

Fontana, E., Mexias, A.S., Renac, C., Nardi, L.V.S., Lopes, R.W., Gomes, M.E.B., Barats, A., 2017. Hydrothermal alteration of volcanic rocks in Seival Mine Cu–mineralization – Camaquã Basin – Brazil (Part I): Chloritization process and geochemical dispersion in alteration halos. Journal of Geochemical Exploration, 177, 45–60.

Fontana, E., Renac, C., Mexias, A.S., Barats, A., Gerbe, M.C., Lopes, R.W., Nardi, L.V.S., 2019. Mass balance and origin of fluids associated to smectite and chlorite/smectite alteration in Seival Mine Cu–Mineralization – Camaquã Basin – Brazil (Part II). Journal of Geochemical Exploration, 196, 20–32.

Franz, G., Spear, F.S., 1985, Aluminous titanite (sphene) from the eclogite zone, south–central Tauern Window, Austria. Chemical Geology, 50, 33–46.

Gastal, M.C.P., Lafon, J.M., Hartmann, L.A., Koester, E., 2005a. Sm–Nd isotopic compositions as a proxy for magmatic processes during the Neoproterozoic of the southern Brazilian shield. Journal of South American Earth Sciences, 18, 255–276.

Gastal, M.C.P., Lafon, J.M., Hartmann, L.A., Koester, E., 2005b. Sm–Nd isotopic investigation of Neoproterozoic and Cretaceous igneous rocks from southern Brazil: a study of magmatic processes. Lithos, 82, 345–377.

Gastal M.C., Lafon, J.M., Ferreira, F.J.F., Magro, F.U.S., Remus, M.V.D., Sommer C.A., 2006. Reinterpretação do Complexo Intrusivo Lavras do Sul – RS, de acordo com os sistemas vulcano–plutônicos de subsidência. Parte I: Geologia, geofísica e geocronologia ($^{207}Pb/^{206}Pb$ e $^{206}Pb/^{238}U$). Revista Brasileira de Geologia (Portuguese – Brazil), 36, 109–124.

Gastal, M.C., Ferreira. F.J.F., Cunha, J.U., Esmeris, C., Koester, E., Raposo, M.I.B., Rossetti, M.M.M., 2015. Lavras granite emplacement and gold mineralization during the development of the post–collisional volcano–plutonic center, west of the Sul–riograndense Shield: Geophysical and structural data. Brazilian Journal of Geology, 45, 217–241.

Ghiorso, M.S., Sack, R.O., 1995. Chemical mass transfer in magmatic processes IV. A revised and internally consistent thermodynamic model for the interpolation and extrapolation of liquid–solid equilibria in magmatic systems at elevated temperatures and pressures. Contributions to Mineralogy and Petrology, 119, 197–212.

Groves, D.I.P., Bierlein, F.P., Meinert, L.D., Hitzman, M.W., 2010. Iron oxide copper–gold (IOCG) deposits through Earth history; implications for origin, lithospheric

676 setting, and distinction from other epigenetic iron oxide deposits. Economic Geology, 105,
677 641–654.
678 Harlov, D.E., Tropper, P., Seifert, W., Nijland, T., Förster, H.–J., 2006. Formation of
679 Al–rich titanite ($CaTiSiO_4O$–$CaAlSiO_4OH$) reaction rims on ilmenite in metamorphic rocks
680 as a function of fH_2O and fO_2. Lithos, 88, 72–84.
681 Hartmann, L.A., Chemale Jr., F., Philipp, R.P., 2007. Evolução Geotectônica do Rio
682 Grande do Sul no Pré–Cambriano. In: Iannuzzi, R., Frantz, J.C. (Eds). 50 anos de Geologia
683 (Portuguese – Brazil). Porto Alegre: Ed. Universidade/UFRGS, pp. 99–123.
684 Higgins, J.B., Ribbe, P.H., 1976. The crystal chemistry and space groups of natural
685 and synthetic titanites. American Mineralogist, 61, 878–888.
686 Hövelmann, J., Putnis, A., Geisler, T., Schmidt, B.C., Golla–Schindler, U., 2010. The
687 replacement of plagioclase feldspars by albite: observations from hydrothermal
688 experiments. Contributions to Mineralogy and Petrology, 159, 43–59.
689 Inoue, A., Utada, M., Nagata, H., Watanabe, T., 1984. Conversion of trioctahedral
690 smectite to interstratified chlorite/smectite in Pliocene acidic pyroclastic sediments of the
691 Ohyu district, Akita Prefecture, Japan. Clay Science, 6, 103–106.
692 Inoue, A., Meunier, A., Patrier–Mas, P., Rigault, C., Beaufort, D., Vieillard, P., 2009.
693 Application of chemical geothermometry to low–temperature trioctahedral chlorites. Clays
694 and Clay Minerals, 57, 371–382.
695 Janikian, L., Almeida, R.P., Trindade, R.I.F., Fragoso–Cesar, A.R.S., D´Agrella–
696 Filho, M.S., Dantas, E.L., Tohver, E., 2008. The continental record of Ediacaran volcano–
697 sedimentary successions in southern Brazil and their global implications. Terra Nova, 20,
698 259–266.
699 Janikian, L., Almeida, R.P., Fragoso–Cesar, A.R.S., Martins, V.T.S., Dantas, E.L.,
700 Tohver, E., McReath, I., D'Agrella–Filho, M.S., 2012. Ages (U–Pb SHRIMP and LA
701 ICPMS) and stratigraphic evolution of the Neoproterozoic volcano–sedimentary
702 successions from the extensional Camaquã Basin, Southern Brazil. Gondwana Research,
703 21, 466–482.
704 Kaur, P., Chaudhri, N., Hofmann, A., Raczek, I., Okrusch, M., Skora, S., 2012. Two–
705 Stage, extreme albitization of A–type granites from Rajasthan, NW India. Journal of
706 Petrology, 53, 919–948.

Kendrick, M.A., Mark, G., Phillips, D., 2007. Mid–crustal fluid mixing in a Proterozoic Fe oxide–Cu–Au deposit, Ernest Henry, Australia: Evidence from Ar, Kr, Xe, Cl, Br and I. Earth and Planetary Science Letters, 256, 328–343.

Kontonikas–Charos, A., Ciobanu, C.L., Cook, N.J., 2014. Albitization and redistribution of REE and Y in IOCG systems: Insights from Moonta–Wallaroo, Yorke Peninsula, South Australia. Lithos, 208–209, 178–201.

Laux, J.H., Lindenmayer, Z.G., Teixeira, J.B.G., Neto, A.B., 2005. Ore genesis at the Camaquã copper mine, a neoproterozoic sediment–hosted deposit in Southern Brazil. Ore Geology Review, 26, 71–89.

Lawrence, M.G., Kamber, B.S., 2006. The behavior of the rare earth elements during estuarine mixing — revisited. Marine Chemistry, 100, 147–161.

Lima, E.F., Nardi, L.V.S., 1998. The Lavras do Sul Shoshonitic Association: implications for origin and evolution of neoproterozoic shoshonitic magmatism in southernmost Brazil. Journal of South American Earth Science, 11, 67–77.

Liz, J.D., Lima, E.F., Nardi, L.V.S., Sommer, C.A., Saldanha, D.L., Pierosan, R., 2009. Petrologia e sucessão estratigráfica das rochas monzoníticas da associação shoshonítica de Lavras do Sul (RS). Revista Brasileira de Geologia (Portuguese – Brazil), 39, 244–255.

Lopes, R.W., Fontana, E., Mexias, A.S., Gomes, M.E.B., Nardi, L.V.S., Renac, C., 2014. Caracterização petrográfica e geoquímica da sequência magmática da Mina do Seival, Formação Hilário (Bacia do Camaquã – Neoproterozoico), Rio Grande do Sul, Brasil. Pesquisas em Geociências (Portuguese – Brazil), 41, 51–64.

Lopes, R.W., Mexias, A.S., Philipp, R.P., Bongiolo, E.M., Renac, C., Bicca, M.M., Fontana, E., 2018. Au-Cu-Ag mineralization controlled by brittle structures in Lavras do Sul Mining District and Seival Mine deposits, Camaquã Basin, southern Brazil. Journal of South American Earth Sciences, 88, 197–215.

Marsh, T.M., Einaudi, M.T., McWilliams, M., 1997. $^{40}Ar/^{39}Ar$ geochronolgy of Cu–Au and Au–Ag mineralization in the Potrerillos district, Chile. Economic Geology, 92, 784-806.

Mark, G., Oliver, N.H.S., Carew, M.J., 2006. Insights into the genesis and diversity of epigenetic Cu–Au mineralization in the Cloncurry district, Mt Isa Inlier, northwest Queensland. Australian Journal of Earth Sciences, 53, 109–124.

Matté, V., Sommer, C.A., Lima, E.F., Philipp, R.P., Basei, M.A.S., 2016. Post–collisional Ediacaran volcanism in oriental Ramada Plateau, southern Brazil. Journal of South American Earth Sciences, 71, 201–222.

McDonough, W.F., Sun, S.S., 1995. Composition of the Earth. Chemical Geology, 120, 223–253.

Mexias, A.S., Formoso, M.L.L., Meunier, A., Beaufort, D., 1990a. O sistema hidrotermal fóssil de Volta Grande – Lavras do Sul/RS. Parte I – Petrografia do hidrotermalismo. Geochimica Brasiliensis (Portuguese – Brazil), 4, 139–157.

Mexias, A.S., Formoso, M.L.L., Gomes, M.E.B., Meunier, A., Beaufort, D., Mattos, I., 1990b. O sistema hidrotermal fóssil de Volta Grande – Lavras do Sul/RS. Parte II – Geoquímica das cloritas. Geochimica Brasiliensis (Portuguese – Brazil), 4, 159–174

Mexias, A.S., Formoso, M.L.L., Meunier, A., Beaufort, D., 1990c. Composition and crystallization of corrensite in volcanic and pyroclastic rocks of Hilário Formation (RS) Brazil. Sciences Géologiques, 88, 135–143.

Mexias, A.S., Berger, G., Gomes, M.E.B., Formoso, M.L.L., Dani, N., Frantz, J.C., Bongiolo, E.M., 2005. Geochemical modelling of gold precipitation conditions in Bloco do Butiá Mine, Lavras do Sul/Brazil. Anais da Academia Brasileira de Ciências (Portuguese – Brazil), 77, 1–12.

Mexias, A.S., Bongiolo, E.M., Gomes, M.E.B., Formoso, M.L.L., Frantz, J.C., 2007. Alterações hidrotermais e mineralizações nas rochas da Associação Plutono– Vulcano–Sedimentar da região de Lavras do Sul–RS. In: Iannuzzi, R., Frantz, J.C. (Eds). 50 anos de Geologia (Portuguese – Brazil). Porto Alegre: Ed. Universidade/UFRGS, pp. 143–159.

Moody, J.B., Jenkins, J.E., Meyer, D., 1985. An experimental investigation of the albitization of plagioclase. Canadian Mineralogist, 23, 583–596.

Oliveira, C.H.E., Chemale Jr., F., Jelinek, A.R., Bicca, M.M., Philipp, R.P., 2014. U–Pb and Lu–Hf isotopes applied to the evolution of the late to post–orogenic transtensional basins of the Dom Feliciano belt, Brazil. Precambrian Research, 246, 240–255.

766 Paim, P.S.G., Chemale Jr., F., Lopes, R.C., 2000. A Bacia do Camaquã. In: Holz, M.;
767 De Ros, L. F. (Ed.). Geologia do Rio Grande do Sul (Portuguese – Brazil). Porto Alegre:
768 Ed. Universidade/UFRGS, pp. 231–374.
769 Parkhurst, D.L, 1995. User's guide to PHREEQC–A computer program for
770 speciation, reaction–path, advective–transport, and inverse geochemical calculations. U.S.
771 Geological Survey Water–Resources Investigations Report, 95–4227, 143 p.
772 Perez, R.J., Boles, J.R., 2005. An empirically derived kinetic model for albitization of
773 detrital plagioclase. American Journal of Science, 305, 312–343.
774 Philipp, R.P., Pimentel, M.M., Chemale Jr., F., 2016. Tectonic evolution of the Dom
775 Feliciano Belt in Southern Brazil: Geological relationships and U–Pb geochronology.
776 Brazilian Journal of Geology, 46, 83–104.
777 Pirajno, F., 2009, Hydrothermal processes and mineral systems. Springer, 1250 p.
778 Reeve, J.S., Cross, K.C., Smith, R.N., Oreskes, N., 1990. Olympic Dam copper–
779 uranium–gold–silver deposit, in Hughes, F. E., ed., Geology of the mineral deposits of
780 Australia and Papua New Guinea: Melbourne, Australasian Institute of Mining and
781 Metallurgy, pp. 1009–1035.
782 Reischl, J.L., 1978. Mineralizações cupriferas associadas a vulcânicas na Mina do
783 Seival. In: XXX Congresso Brasileiro De Geologia (Portuguese – Brazil), Recife. Anais,
784 SBG, 4, 1568–1582.
785 Remus, M.D.V., Hartmann, L.A., McNaughhton, M.J., Fletcher, I.R., 1999. Shrimp
786 U–Pb zircon ages of volcanism from the São Gabriel Block, southern Brazil. In: Simpósio
787 sobre vulcanismo e ambientes associados, 1. Boletim de Resumos, 83 p.
788 Remus, M.V.D., Hartmann, L.A., McNaughton, N.J., Groves, D.I., Reischl, J.L.,
789 2000. A distal magmatic–hydrothermal origin for the Camaquã Cu (Au–Ag) and Santa
790 Maria Pb, Zn (Cu–Ag) deposits, southern Brazil. Gondwana Research, 3, 155–174.
791 Renac, C., Mexias, A.S., Gomes, M.E.B., Ronchi, L.H., Nardi, L.V.S., Laux, J.H.,
792 2014. Isotopic fluid changes in a Neoproterozoic porphyry–epithermal system: the Uruguay
793 mine, southern Brazil. Ore Geology Review, 60, 146–160.
794 Ribeiro, M., Fantinel, L.M., 1978. Associacões petrotectônicas do Escudo Sul–
795 Riograndense: I Tabulação e distribuicão das associações petrotectônicas do Escudo do Rio
796 Grande do Sul. Inheringia Serviço Geológico (Portuguese – Brazil), 5, 19–54.

797 Richards, J.P., 2003. Tectono–magmatic precursors for porphyry Cu–(Mo–Au)
798 deposit formation. Economic Geology, 98, 1515–1533.
799 Salve, P.R., Maurya, A., Wate, S.R., Devotta, S., 2008. Chemical composition of
800 major ions in rainwater. Bulletin of Environmental Contamination and Toxicology, 80,
801 242–246.
802 Seedorff, E., Dilles, J.H., Proffett Jr., J.M., Einaudi, M.T., Zurcher, L., Stavast,
803 W.J.A., Johnson, D.A., Barton, M.D., 2005. Porphyry deposits: characteristics and origin of
804 hypogene features. Society of Economic Geologists, Economic Geology 100th Anniversary
805 Volume, 251–298.
806 Sillitoe, R.H., 1991. Gold metallogeny of Chile – an introduction: Economic
807 Geology, 86, 1187–1205.
808 Sillitoe, R.M., 2003. Iron oxide–copper–gold deposits: An Andean view. Mineralium
809 Deposita, 38, 787–812.
810 Sillitoe, R.H., 2010, Porphyry copper systems. Economic Geology, 105, 3–41.
811 Silva, L.C., McNaughton, N.J., Armstrong R., Hartmann, L.A., Fletcher, I.R., 2005.
812 The neoproterozoic Mantiqueira Province and its African connections: a zircon based U–Pb
813 geochronologic subdivision for the Brasiliano/Pan–African systems of orogens.
814 Precambrian Research, 136, 203–240.
815 Sommer, C.A., Lima, E.F., Nardi, L.V.S., Figueiredo, A.M.G., Pierosan, R., 2006.
816 Potassic and Low–and High–Ti mildly alkaline volcanism In the Neoproterozoic Ramada
817 Plateau, Southermost Brazil. Journal of South American Earth Sciences, 18, 237–254.
818 Taylor, B.E., 1987. Stable isotope geochemistry of ore–forming fluids. In: Kyser, T.K.
819 (Ed.), Stable isotope geochemistry of low temperature processes. Mineralogical Association
820 of Canada, Short Course Handbook, 13, 337–445.
821 Toniolo, J.A., Gil, C.A.A., Sander, A., 2007. Projeto BANEO–Metalogenia das
822 Bacias Neoproterozóico–Eopaleozóicas do Sul do Brasil – Bacia do Camaquã. CPRM –
823 Serviço Geológico do Brasil (Portuguese – Brazil), CD Rom.
824 Troian, G.C., Mexias, A.S., Gomes, M.E.B., Canarim, D., Patricia Patrier–Mas, P.,
825 Renac, C., 2010. Cloritização na Mina Uruguai, Minas do Camaquã, RS, Brasil. Pesquisas
826 em Geociências (Portuguese – Brazil), 37, 173–190.

Tropper, P., Manning, C.E., Essene, E.J., 2002. The substitution of Al and F in titanite at high pressure and temperature: experimental constraints on phase relations and solid solution properties. Journal of Petrology, 43, 1787–1814.

Velde, B., 1985. Clay minerals: a physico–chemical explanation of their occurrence. Developments in Sedimentology, 40, Elsevier, Amsterdam, 427 p.

Wiewióra, A., Weiss, Z., 1990. Crystallochemical classifications of phyllosilicates based on the unified system of projection of chemical composition: II The chlorite group. Clay Minerals, 25, 83–92.

Wilkinson, J.J., Chang, Z., Cooke, D.R., Baker, M.J., Wilkinson, C.C., Inglis, S., Chen, H., Gemmell, J.B., 2015. The chlorite proximitor: A new tool for detecting porphyry ore deposits. Journal of Geochemical Exploration, 152, 10–26.

Williams, P.J., Barton, M.D., Johnson, D.A., Fontboté, L., de Haller, A., Mark, G., Oliver, N.H.S., Marschik, R., 2005. Iron oxide copper–gold deposits: Geology, Space–time distribution, and possible modes of origin. Economic Geology, 100th Anniversary Volume, 371–405.

Worrall, F., Pearson, D.G., 2001. Water–rock interaction in an acidic mine discharge as indicated by rare earth element patterns. Geochimica et Cosmochimica Acta, 65, 3027–3040.

Yoneda, T., Watanabe, T., Sato, T., 2016. Mineralogical aspects of interstratified chlorite–smectite associated with epithermal ore veins: A case study of the Todoroki Au–Ag ore deposit, Japan. Clay Minerals, 51, 653–674.

Figures and Tables Legends

Figure 1. Geological setting of the study area. A) Schematic Sul–rio–grandense Shield map (modified from Hartmann et al., 2007); B) Central–western Camaquã Basin geological map with Seival Mine area and Cu occurrences localization (modified from Toniolo et al., 2007; Gastal et al., 2015). Keys: 1= Seival Mine (Cu and Ag); 2= Silveira Mine (Cu); 3= Crespos Mine (Cu); 4= Volta Grande and Merita Mine (Cu and Au).

Figure 2. Geological map of the Seival Mine. Sequence of lapilli tuff, andesitic lava flows and volcanic agglomerate with andesitic and trachyandesitic dike (NE direction) from Hilário Formation (HF), polymictic conglomerate and vesicular lava flows from Santa Fé Formation (SFF), rhyolite dikes of Acampamento Velho Formation (AVF), faults, mineralization projections, inactive open pit mines and bore–hole localization (modified from Reischl, 1978; Lopes et al., 2014). Keys: 1= Barita Mine; 2= João Dahne Mine; 3= Morcego Mine; 4= Meio Mine; 5= Cruzeta Mine; 6= Alcides Mine.

Figure 3. Mineralization in the Seival Mine area. A) Cu soil anomaly (modified from Reischl, 1978) and inactive open pit mines, faults and Cu–mineralization; B) Schematic section of alteration zones in Hilário Formation. Keys: Chl= Chlorite; C/S= Chlorite/smectite mixed–layer; Hem= Hematite; Tit= Titanite; Cal= Calcite; Qtz= Quartz; Cc= Chalcocite; Bn= Bornite; Smec= Smectite.

Figure 4. Macroscopic photograph (A and B), photomicrograph in natural (C and F) and polarized light (D, E, G and H). A) Hand sample containing altered pyroclasts of lapilli tuff; B) Hand sample with plagioclase and altered groundmass in andesite dike; C) Pervasive clay minerals alteration in lapilli tuff; D) Zoned phenocryst of plagioclase with indication of unaltered andesine–labradorite and altered plagioclase with albite composition in andesitic dike; E) Clinopyroxene and vesicle fulfilled by smectite–rich chlorite/smectite in less altered amygdaloidal andesitic lava flows; F) Amygdaloidal andesitic lava flows pyroclast of lapilli tuff fulfilled by chlorite, calcite, sulfide, titanite and quartz; G) Smectite in less altered andesitic lava flows; H) Vesicle fulfilled by chlorite/smectite mixed–layers in andesitic lava flows. Keys: Pl= Plagioclase; Sul= Sulfide; Cal= Calcite; Tit= Titanite;

Hem= Hematite; Qtz= Quartz; K–fds= K–feldspar; And–lab= Andesine–labradorite; Ab= Albite; C/S= Chlorite/smectite mixed–layer; Px= Pyroxene; Chl= Chlorite, Smec= Smectite.

Figure 5. Plots of mineral compositions. A) Ca–Mg–Fe clinopyroxenes showing augite compositions in andesitic lava flows and andesitic dike; B) Biotite (white point) and less pristine biotite (gray point) in the Al_{tot} *vs* Al^{VI} diagram; C) Al+Fe^{3+} *vs* Ti and Al *vs* Fe binary diagram of the hydrothermal titanite compositions (diagram extracted from Cao et al., 2015); D) An–Ab–Or ternary feldspar diagram showing albitization in andesine–labradorite and rims with K–feldspar in some zoned plagioclase (An= Anorthite; Ab= Albite; Or= Orthoclase).

Figure 6. Chemical compositions of a series of saponite, chlorite and chlorite/smectite mixed–layers in projection M^{+}, 4Si and $3R^{2+}$ (Velde, 1985; adapted from Inoue et al., 1984) with detail showing the smectite, chlorite–rich chlorite–smectite mixed–layer (C/S) and chlorite compositions from Seival Mine, as well as comparison between chlorites analyzes from epithermal Lavras do Sul (Mexias et al., 1990b, c; Bongiolo et al., 2011) and Camaquã Mine (Renac et al., 2014).

Figure 7. Atomic proportions of chlorites in vein and groundmass of andesitic dikes presented in Wiewiora and Weiss diagram (1990), of Si and divalent transition metals normalized to chlorite atom per formula (28 oxygen total anions atoms) in comparison with epithermal system from Lavras do Sul (Mexias et al., 1990b; Bongiolo et al., 2011) and Camaquã Mine (Renac et al., 2014) and graphical representation of low–temperature chlorite geothermometry (Bourdelle and Cathelineau, 2015).

Figure 8. X–ray diffraction patters of < 0.4 μm clay–size fraction of chlorite (A), corrensite (B), smectite (C) and chlorite/smectite (C/S) mixed–layer (D). Keys: Air dried (black line); EG= Ethylene glycol solvation (gray line); Heating treatment (light gray line); Chl= Chlorite; Smec= Smectite.

Figure 9. S.E.M. images obtained from drill hole fresh rock sample fragment of amygdaloidal andesitic lava flows described by Fontana et al. (2017). A) Albite fragment associated with corrensite clay minerals of the andesitic lava flows groundmass; B) Detail of corrensite morphology of the altered andesitic lava flows groundmass. Keys: Ab= Albite; Cor= Corrensite.

Figure 10. REE normalized patterns by the chondrite values (McDonough and Sun, 1995). A) Andesine–labradorite with slight albitization of group I; B) Albite–rich plagioclases of group II.

Table 1. Summary of mineral, host rock and structural formula of magmatic, magmatic to late–magmatic and hydrothermal phases. Nomenclature of chlorites after Bayliss (1975).

Table 2. Measured REE analyzes and normalized values to McDonough and Sun (1995) in separate plagioclase grains of the Seival Mine, andesitic lava flows located outside of the area (black line) and whole–rock analyzes (Lopes et al., 2014). Keys: And= Andesitic lava flows; AD= Andesitic dike; Outs. area= Andesitic lava flows located of outside studied area; Light REE= La to Sm; Heavy REE= Eu to Lu; ΣREE= Sum of total concentration of not normalized rare earth elements; Eu*= The value of the Eu anomaly calculated by the formula $[Eu^*]= [((Eu_N)/(Sm_N \times Gd_N)^{1/2})]$ from Worrall and Pearson (2001) or $[Eu^*]= [((Eu_N)/(Sm_N^2 \times Tb_N)^{1/3})]$ from Lawrence and Kamber (2006).

Supplementary Table. Representative compositions of pyroxene (A), biotite (B), titanite (C), feldspar (D) and clay minerals as chlorite (E), smectite (F) and chlorite/smectite mixed–layer (G) analyzes and structural formula. Chlorite temperatures values are showed in Supplementary Table E (Inoue et al., 2009; Bourdelle and Cathelineau, 2015).

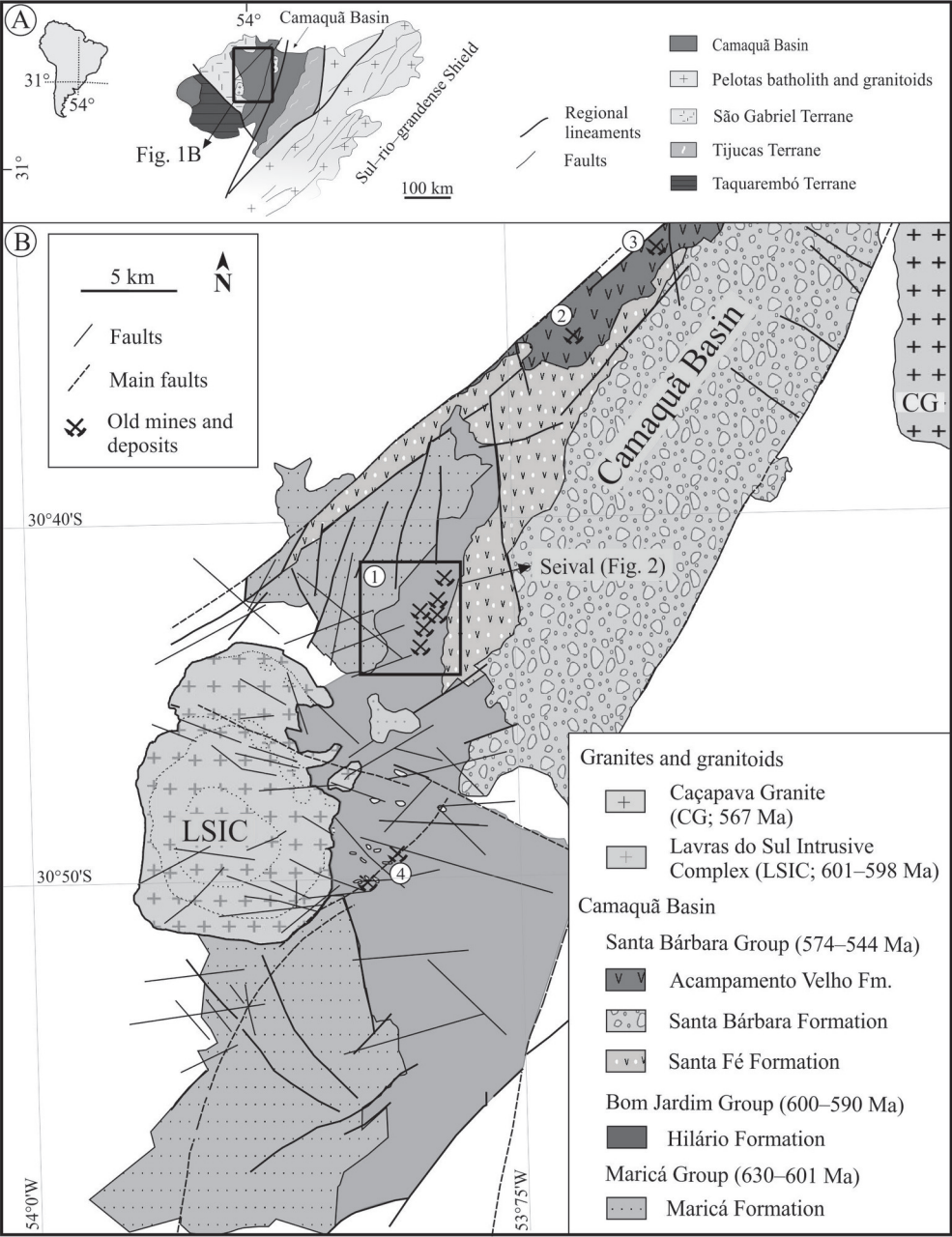
A
54°
Camaquã Basin
31°
54°
31°
Fig. 1B
Sul-rio-grandense Shield
100 km
Regional lineaments
Faults
Camaquã Basin
Pelotas batholith and granitoids
São Gabriel Terrane
Tijucas Terrane
Taquarembó Terrane
B
5 km
N
Faults
Main faults
Old mines and deposits
Camaquã Basin
CG
Seival (Fig. 2)
LSIC
30°40'S
30°50'S
54°0'W
53°75'W
Granites and granitoids
Caçapava Granite (CG; 567 Ma)
Lavras do Sul Intrusive Complex (LSIC; 601–598 Ma)
Camaquã Basin
Santa Bárbara Group (574–544 Ma)
Acampamento Velho Fm.
Santa Bárbara Formation
Santa Fé Formation
Bom Jardim Group (600–590 Ma)
Hilário Formation
Maricá Group (630–601 Ma)
Maricá Formation

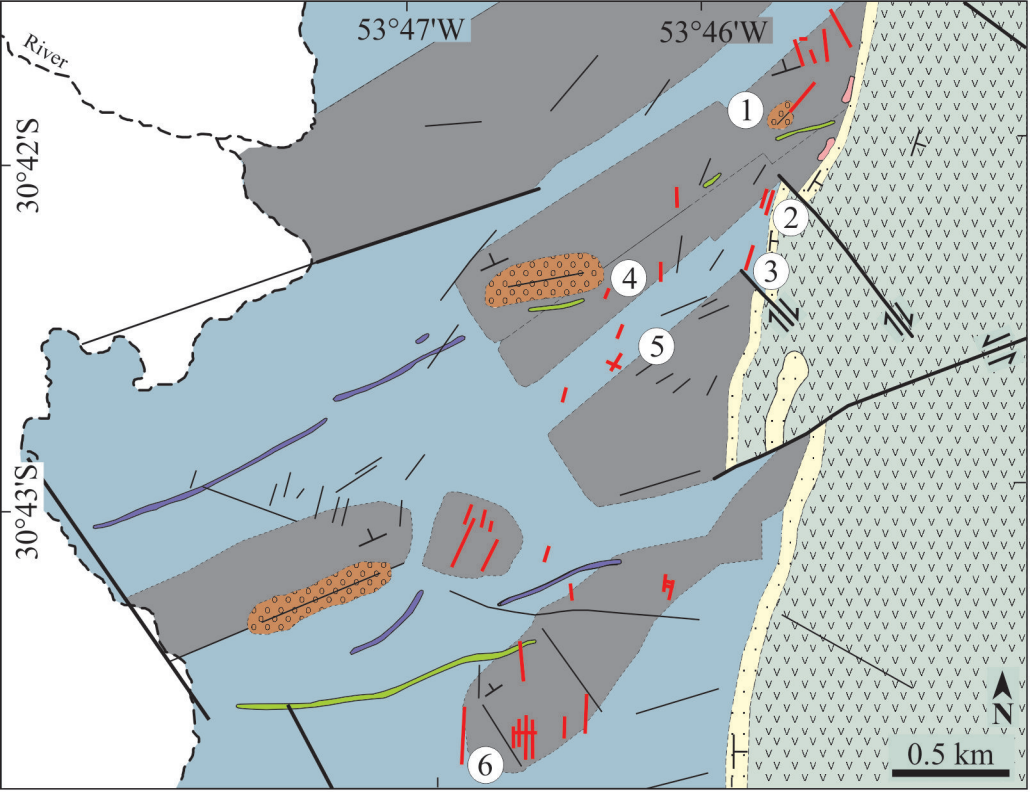

CAMAQUÃ BASIN (630–540 Ma)

Santa Bárbara Group (574–544 Ma)

Acampamento Velho Formation

Rhyolite dike

Santa Fé Formation

Polimitic conglomerate

Vesicular lava flows

Bom Jardim Group (600–590 Ma)

Hilário Formation

Trachyandesite dike

Andesite dike

Volcanic agglomerate

Andesitic lava flow

Lapilli tuff

Legend

Faults

Main faults

Mineralization

River

Dipping (S0)

Inactive mine

1 Barita

2 João Dahne

3 Morcego

4 Meio

5 Cruzeta

6 Alcides

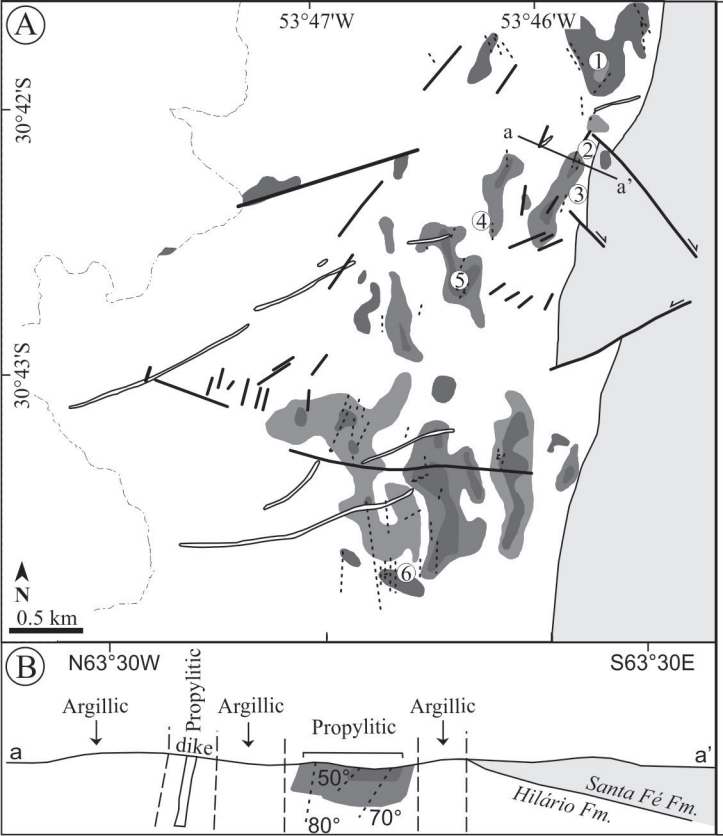

CAMAQUÃ BASIN

- Santa Fé Formation
- Dikes
- Hilário Formation
- Mineralization projections
- Fault
- River

Copper soil anomaly

- > 120 ppm
- 101-120 ppm
- 81-100 ppm
- *< 80 ppm (background)*

Mine	Cu	Ag
1. Barita	1.71%	70 ppm
2. João Dahne		
3. Morcego	2.5%	
4. Meio	0.6%	15 ppm
5. Cruzeta		
6. Alcides	0.83%	16 ppm

ALTERATION ZONES

Propylitic
Chl+C/S+Hem+Tit+Cal+Qtz

Argillic
Smec+Qtz

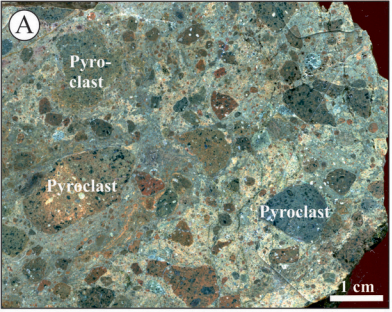
A
Pyro-
clast
Pyroclast
Pyroclast
1 cm

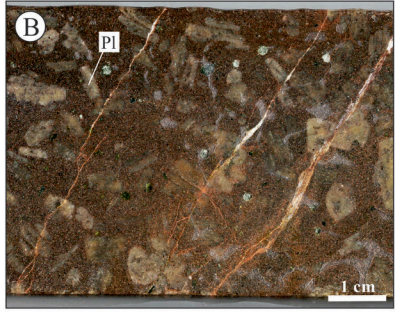
B
Pl
1 cm

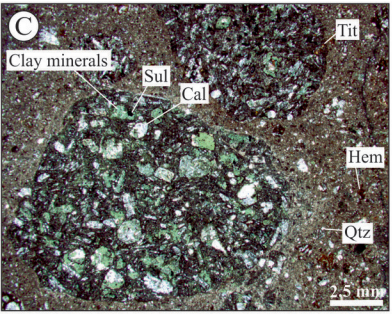
C
Tit
Clay minerals
Sul
Cal
Hem
Qtz
2.5 mm

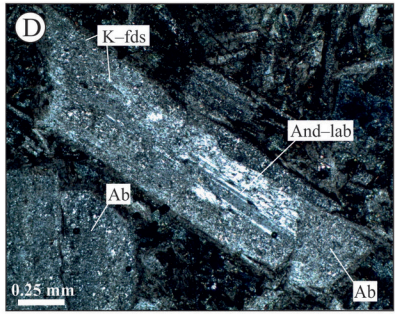
D
K–fds
And–lab
Ab
0.25 mm
Ab

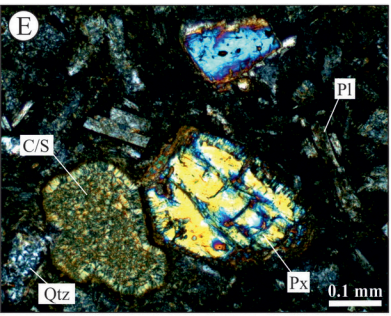
E
Pl
C/S
Qtz
Px
0.1 mm

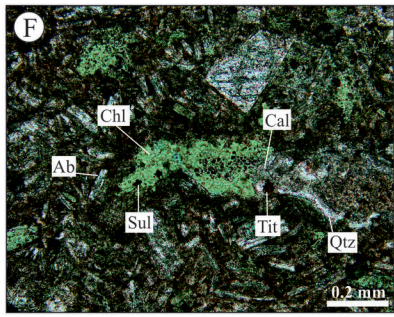
F
Chl
Cal
Ab
Sul
Tit
Qtz
0.2 mm

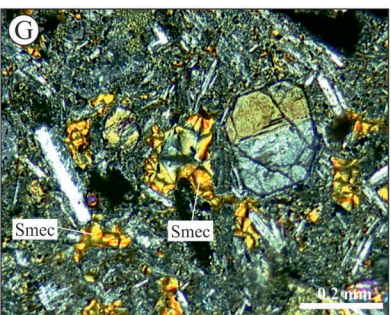
G
Smec
Smec
0.2 mm

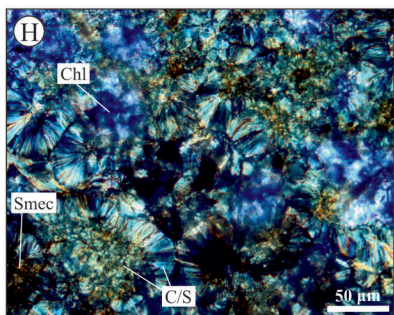
H
Chl
Smec
C/S
50 μm

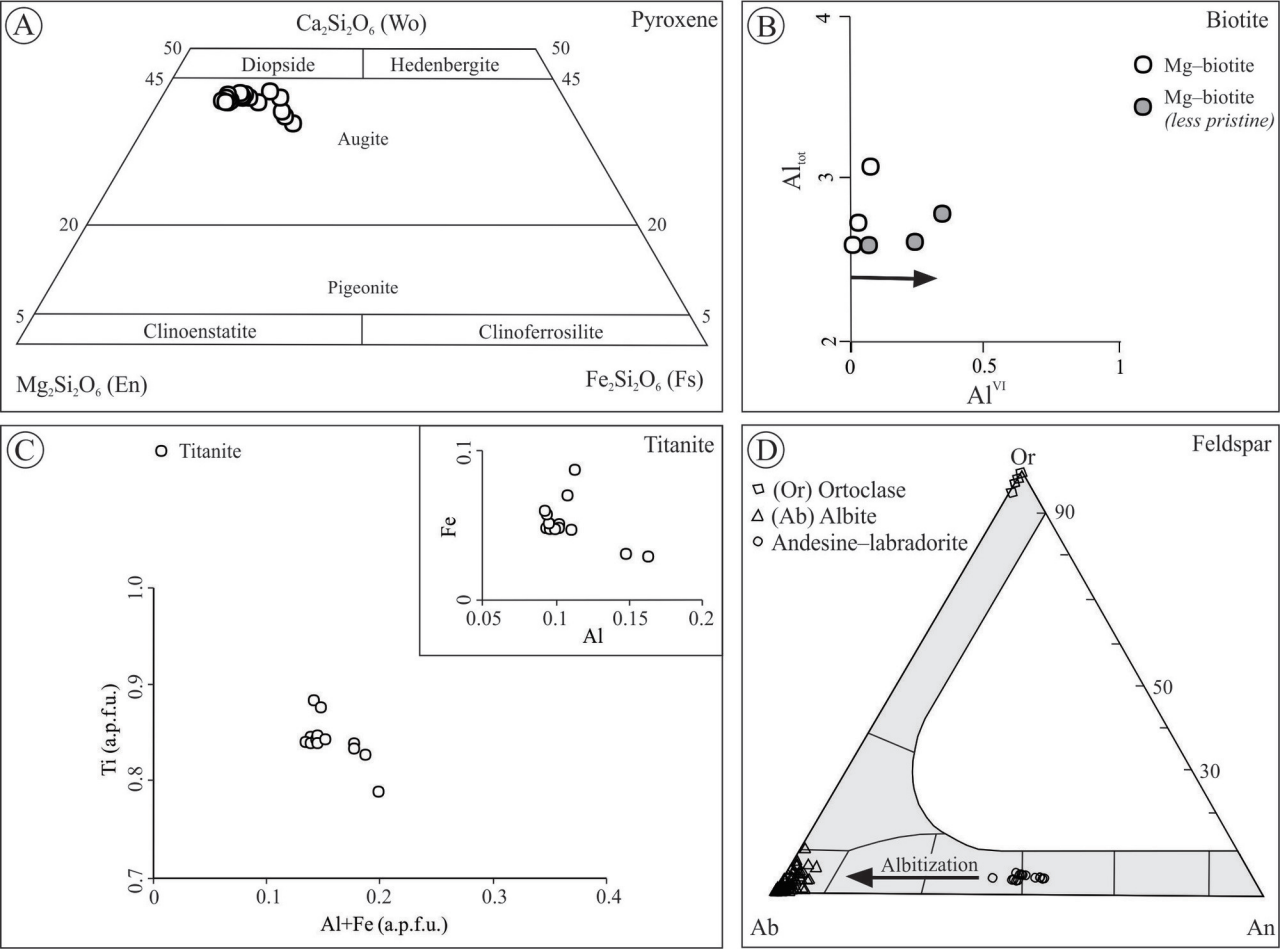
A
Pyroxene
$Ca_2Si_2O_6$ (Wo)
50
45
20
5
Diopside
Hedenbergite
Augite
Pigeonite
Clinoenstatite
Clinoferrosilite
$Mg_2Si_2O_6$ (En)
$Fe_2Si_2O_6$ (Fs)
B
Biotite
Mg–biotite
Mg–biotite
(less pristine)
Al_{tot}
Al^{VI}
C
Titanite
Ti (a.p.f.u.)
Al+Fe (a.p.f.u.)
Fe
Al
D
Feldspar
(Or) Ortoclase
(Ab) Albite
Andesine–labradorite
Or
Ab
An
Albitization

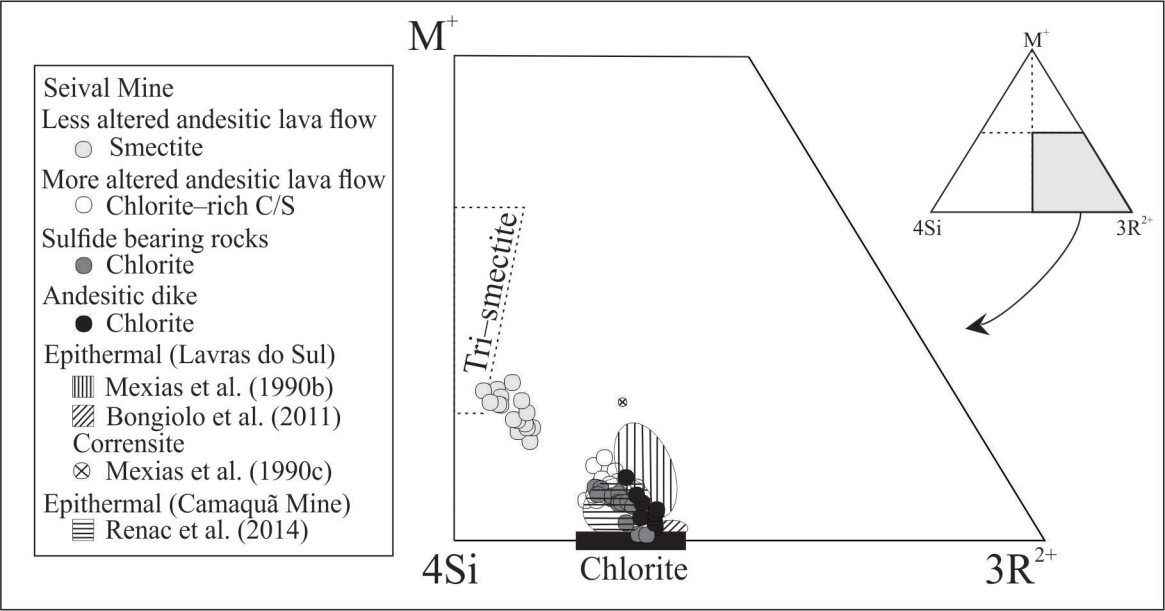
Seival Mine
Less altered andesitic lava flow
Smectite
More altered andesitic lava flow
Chlorite–rich C/S
Sulfide bearing rocks
Chlorite
Andesitic dike
Chlorite
Epithermal (Lavras do Sul)
Mexias et al. (1990b)
Bongiolo et al. (2011)
Corrensite
Mexias et al. (1990c)
Epithermal (Camaquã Mine)
Renac et al. (2014)
M+
Tri–smectite
4Si
Chlorite
3R2+
M+
4Si
3R2+

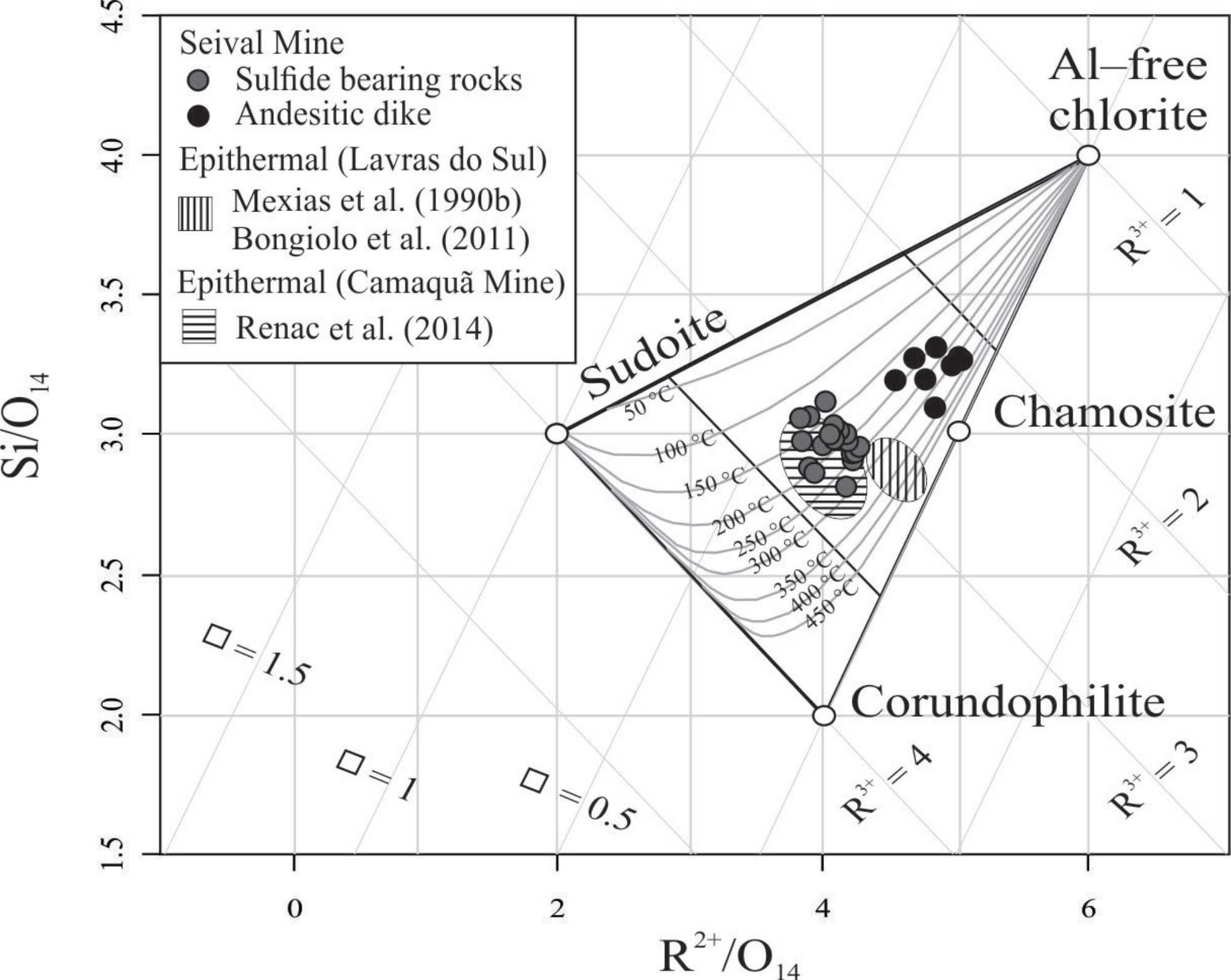
Seival Mine
Sulfide bearing rocks
Andesitic dike
Epithermal (Lavras do Sul)
Mexias et al. (1990b)
Bongiolo et al. (2011)
Epithermal (Camaquã Mine)
Renac et al. (2014)
Al–free chlorite
Sudoite
Chamosite
Corundophilite
50 °C
100 °C
150 °C
200 °C
250 °C
300 °C
350 °C
400 °C
450 °C
□ = 1.5
□ = 1
□ = 0.5
R3+ = 1
R3+ = 2
R3+ = 3
R3+ = 4
Si/O14
R2+/O14
4.5
4.0
3.5
3.0
2.5
2.0
1.5
0
2
4
6

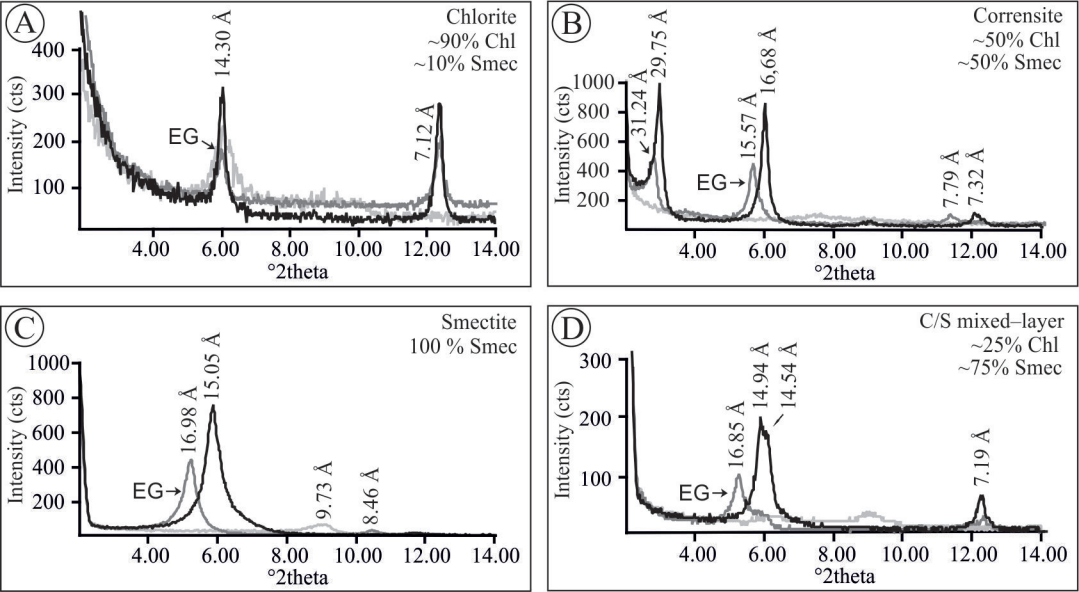
A
Chlorite
~90% Chl
~10% Smec
14.30 Å
7.12 Å
EG
Intensity (cts)
400
300
200
100
4.00
6.00
8.00
10.00
12.00
14.00
°2theta
B
Corrensite
~50% Chl
~50% Smec
29.75 Å
31.24 Å
16,68 Å
15.57 Å
7.79 Å
7.32 Å
EG
Intensity (cts)
1000
800
600
400
200
4.00
6.00
8.00
10.00
12.00
14.00
°2theta
C
Smectite
100 % Smec
16.98 Å
15.05 Å
9.73 Å
8.46 Å
EG
Intensity (cts)
1000
800
600
400
200
4.00
6.00
8.00
10.00
12.00
14.00
°2theta
D
C/S mixed–layer
~25% Chl
~75% Smec
16.85 Å
14.94 Å
14.54 Å
7.19 Å
EG
Intensity (cts)
300
200
100
4.00
6.00
8.00
10.00
12.00
14.00
°2theta

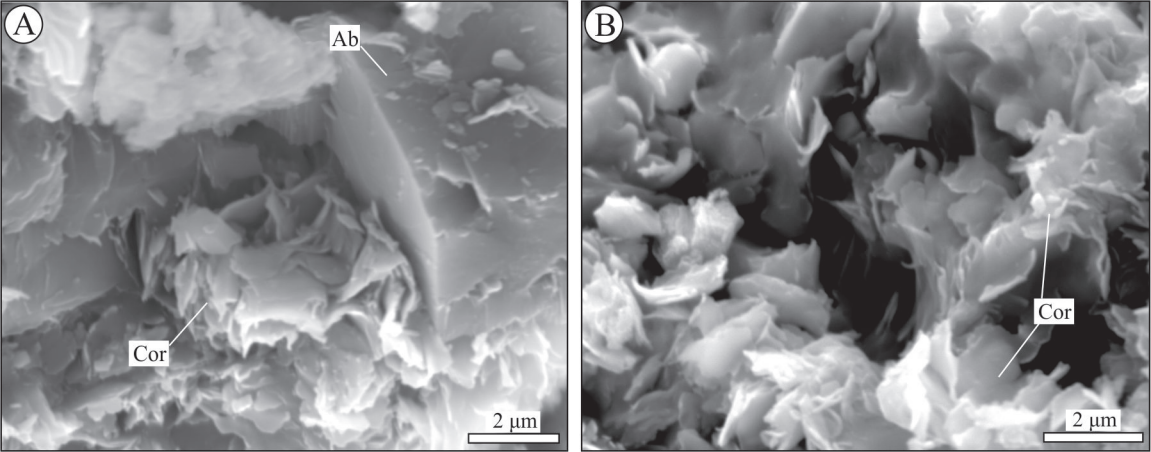
A
Ab
Cor
2 µm
B
Cor
2 µm

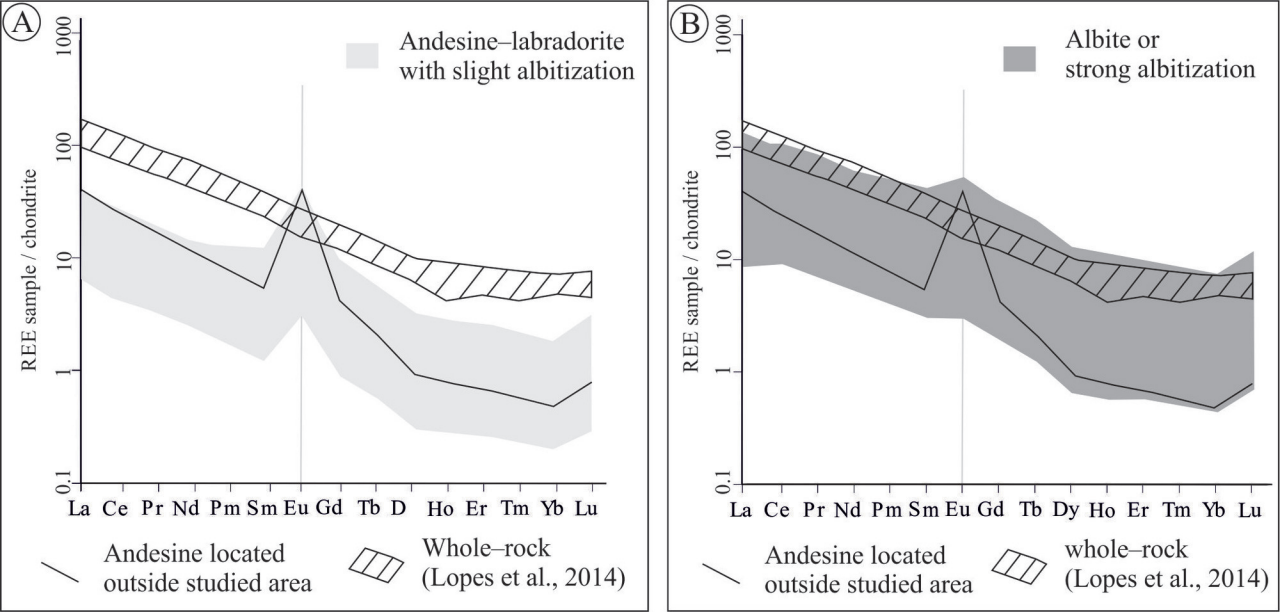
A
Andesine–labradorite
with slight albitization
REE sample / chondrite
1000
100
10
1
0.1
La Ce Pr Nd Pm Sm Eu Gd Tb D Ho Er Tm Yb Lu
Andesine located
outside studied area
Whole–rock
(Lopes et al., 2014)
B
Albite or
strong albitization
REE sample / chondrite
1000
100
10
1
0.1
La Ce Pr Nd Pm Sm Eu Gd Tb Dy Ho Er Tm Yb Lu
Andesine located
outside studied area
whole–rock
(Lopes et al., 2014)

Host rock	Mineral	Structural formula
Magmatic phase		
Andesitic lava flow and dike: less altered	Augite	$[(Ca_{0.70–0.81}Na_{0.01–0,03})(Fe^{+2}_{0.15–0.32}Mg_{0.86–0.97})(Al_{0.06–0.19}Ti_{0–0.02}Fe^{+3}_{0–0.06})(Si_{1.88–1.99})O_{12}]$
Trachyandesitic dike: magmatic or pristine	Mg–biotite	$[(Ca_{0.01–0.03}Na_{0.09–0.25}K_{0.61–1.41})(Fe^{+2}_{1.92–2.3}Mg_{2.95–3.81}Mn_{0.01–0.03}Al_{0–0.07}Ti_{0.44–0.76})^{VI}(Al_{2.61–2.98}Si_{5.02–5.39})^{IV}O_{20}OH_{3.75–3.96}F_{0.03–0.25}]$
Trachyandesitic dike: less pristine	Mg–biotite	$[(Ca_{0.01–0.02}Na_{0.20–0.24}K_{1.22–1.49})(Fe^{+2}_{1.79–2.02}Mg_{2.72–2.89}Mn_{0.01–0.02}Al_{0.07–0.33}Ti_{0.61–0.75})^{VI}(Al_{2.39–2.54}Si_{5.46–5.61})^{IV}O_{20}OH_{3.73–3.85}F_{0.15–0.27}]$
Magmatic to late–magmatic phase		
Andesitic dike: euehdral to agglomerates	Titanite	$[(Ca_{0.94–1.02}\square_{0.02}Ti_{0.79–0.88}Al_{0.09–0.16}Fe^{3+}_{0.03–0.09}Mg_{0–0.03}Si_{1.01–1.07}O_5)]$
Andesitic dike and lava flow: less altered	Andesine–labradorite	$[(An_{0.43–0.53}Ab_{0.43–0.54}Or_{0.03–0.05})]$
Andesitic dike	K–feldspar	$[(An_{0.43–0.53}Ab_{0.43–0.54}Or_{0.03–0.05})]$
Andesitic lava flow and dike: more altered	Albite	$[(An_{0–0.06}Ab_{0.89–1}Or_{0–0.10})]$
Hydrothermal phase		
* Porphyritic andesitic lava flow: augite replacement	Mg–chamosite to Fe–clinochlore	$[(Ca_{0.04–0.06}Na_{0–0.04}K_{0.02–0..11})(Al_{2.70–3.03}Ti_{0–0.01}Fe^{3+}_{0.37–0.57}Fe^{2+}_{3.61–5.23}Mg_{3.07–3.97}Mn_{0.01–0.04})^{VI}(Si_{5.94–6.24}Al_{1.76–2.06})^{IV}O_{20}(OH)_8]$
** Lapilli tuff: filled vugs	Mg–chamosite	$[(Ca_{0–0.03}Na_{0–0.04}K_{0–0.11})(Al_{2.70–3.11}Ti_{0–0.01}Fe^{3+}_{0.31–0.46}Fe^{2+}_{4.38–5.14}Mg_{3.17–3.50}Mn_{0.01–0.02})^{VI}(Si_{5.62–6.01}Al_{1.99–2.38})^{IV}O_{20}(OH)_8]$
*** Andesitic dikes: matrix	Mg–chamosite to Fe–clinochlore	$[(Ca_{0.03–0.12}Na_{0–0.03}K_{0.01–0.05})(Al_{1.63–2.13}Ti_{0–0.01}Fe^{3+}_{0.1–0.28}Fe^{2+}_{4.26–5.49}Mg_{4.4–4.74}Mn_{0.03–0.08})^{VI}(OH)_4(Si_{6.20–6.62}Al_{1.38–1.80})^{IV}O_{20}(OH)_8)]$
Amygdaloidal andesitic lava flow: less altered rocks	Mg–saponite	$[(Ca_{0.18–0.31}Na_{0.02–0.05}K_{0.02–0.07})(Al_{0.06–0.23}Ti_{0–0.01}Fe^{+2}_{1.35–1.78}Mg_{4.50–4.81}Mn_{0.02–0.03})^{VI}(Si_{6.41–6.98}Al_{1.02–1.59})^{IV}O_{20}(OH)_2]$
Amygdaloidal andesitic lava flow: less altered rocks	Chl–rich C/S mixed–layer	$[(Ca_{0.05–0.16}Na_{0–0.09}K_{0.01–0.05})(Al_{1.59–1.93}Ti_{0–0.01}Fe^{3+}_{0.18–0.49}Fe^{2+}_{2.68–3.77}Mg_{5.70–6.37}Mn_{0.03–0.05})^{VI}(Si_{6.53–7.23}Al_{0.77–1.47})^{IV}O_{20}(OH)_8]$
Porphyritic andesitic lava flow: more altered rock	Chl–rich C/S mixed–layer	$[(Ca_{0.05–0.07}Na_{0.02–0.06}K_{0.01–0.03})(Al_{2.21–2.46}Ti_{0–0.02}Fe^{3+}_{0.46–0.61}Fe^{2+}_{2.19–2.74}Mg_{5.59–5.86}Mn_{0.06–0.07})^{VI}(Si_{6.52–6.75}Al_{1.25–1.48})^{IV}O_{20}(OH)_8]$

Sample (mg/kg)	FM 13	DD 62	RFM 66	RFM 55	WL 13	WL 19	FM 33	FM 32	DD 76	RFM 68
	Group I			Group II						Outs. Area
	AD	AD	AD	And	And	And	AD	AD	AD	And
Y	0.23	1.61	1.63	9.18	3.15	2.26	0.41	1.36	11.03	1.24
La	1.66	6.18	9.95	28.39	7.70	5.47	2.16	4.30	31.66	8.09
Ce	2.68	15.41	17.54	55.31	19.25	16.08	5.57	14.19	60.18	13.61
Pr	0.32	1.65	1.90	8.15	2.29	2.06	0.66	1.89	7.79	1.46
Nd	1.14	6.10	6.54	32.46	8.71	8.07	2.51	7.31	29.43	5.04
Sm	0.18	1.77	1.51	5.85	2.12	2.25	0.45	2.61	6.47	0.82
Eu	0.17	1.79	2.36	2.28	0.60	0.67	0.17	0.82	3.05	1.75
Gd	0.18	1.89	1.62	5.55	1.94	1.92	0.37	2.19	6.50	0.90
Tb	0.02	0.21	0.17	0.74	0.26	0.26	0.04	0.28	0.81	0.09
Dy	0.07	0.78	0.58	3.07	1.11	1.05	0.16	1.04	3.20	0.30
Ho	0.02	0.15	0.11	0.65	0.23	0.21	0.03	0.20	0.63	0.06
Er	0.04	0.40	0.31	1.80	0.59	0.56	0.09	0.54	1.64	0.16
Tm	0.01	0.06	0.04	0.28	0.09	0.09	0.01	0.08	0.24	0.02
Yb	0.03	0.29	0.22	1.46	0.45	0.45	0.07	0.39	1.21	0.11
Lu	0.01	0.08	0.05	0.35	0.12	0.12	0.02	0.12	0.29	0.03
Normalization standard CI chondrite (McDonough and Sun, 1995)										
La_N	6.99	26.07	42.00	119.77	32.50	23.10	9.10	18.16	133.6	34.12
Ce_N	4.37	25.14	28.62	90.23	31.40	26.23	9.09	23.15	98.18	22.21
Pr_N	3.41	17.80	20.48	87.81	24.68	22.19	7.12	20.42	83.91	15.70
Nd_N	2.49	13.35	14.32	71.04	19.06	17.66	5.48	16.01	64.4	11.03
Sm_N	1.20	11.98	10.22	39.55	14.32	15.20	3.02	17.66	43.73	5.53
Eu_N	3.04	31.85	41.95	40.48	10.57	11.87	2.98	14.55	54.09	31.07
Gd_N	0.89	9.50	8.14	27.90	9.74	9.66	1.88	10.98	32.67	4.50
Tb_N	0.55	5.73	4.63	20.44	7.31	7.15	1.22	7.73	22.49	2.41
Dy_N	0.30	3.16	2.35	12.48	4.50	4.26	0.64	4.24	13.02	1.21
Ho_N	0.27	2.71	2.03	11.83	4.12	3.83	0.57	3.70	11.45	1.04
Er_N	0.26	2.51	1.94	11.27	3.69	3.53	0.56	3.39	10.26	0.98
Yb_N	0.20	1.82	1.37	9.09	2.80	2.81	0.43	2.43	7.54	0.69
Lu_N	0.28	3.09	2.15	14.27	4.72	4.88	0.69	4.67	11.91	1.06
ΣLREE	5.98	31.11	37.44	130.16	40.07	33.93	11.35	30.30	135.53	29.02
ΣHREE	0.55	5.65	5.46	16.18	5.39	5.33	0.96	5.66	17.57	3.42
ΣREE	6.76	38.37	44.53	155.52	48.61	41.52	12.72	37.32	164.13	33.68
$[Eu^*]= [((Eu_N)/(Sm_N \times Gd_N)^{1/2})]$	1.22	0.90	0.98	2.94	2.99	4.60	1.25	1.04	1.43	6.23
$[Eu^*]= [((Eu_N)/(Sm_N^{2} \times Tb_N)^{1/3})]$	1.28	0.92	1	3.29	3.40	5.35	1.33	1.09	1.54	7.41